https://doi.org/10.5194/egusphere-2025-1942
Preprint. Discussion started: 24 June 2025

Results of the second Ice Shelf – Ocean Model Intercomparison Project (ISOMIP+)

Claire K. Yung[1], Xylar S. Asay-Davis[2], Alistair Adcroft[3], Christopher Y. S. Bull[4], Jan De Rydt[5], Michael S. Dinniman[6], Benjamin K. Galton-Fenzi[7,8], Daniel Goldberg[9], David E. Gwyther[10], Robert Hallberg[3,11], Matthew Harrison[11], Tore Hattermann[12], David M. Holland[13], Denise Holland[13], Paul R. Holland[14], James R. Jordan[15], Nicolas C. Jourdain[16], Kazuya Kusahara[17], Gustavo Marques[18], Pierre Mathiot[16], Dimitris Menemenlis[19], Adele K. Morrison[1], Yoshihiro Nakayama[20,21], Olga Sergienko[3], Robin S. Smith[22], Alon Stern[3], Ralph Timmermann[23], and Qin Zhou[24]

[1]Research School of Earth Sciences and Australian Centre for Excellence in Antarctic Science, The Australian National University, Canberra, Australia
[2]Fluid Dynamics and Solid Mechanics, Los Alamos National Laboratory, Los Alamos, NM 87545, USA
[3]Atmospheric and Oceanic Sciences Program, Princeton University, Princeton, NJ, USA
[4]ACCESS-NRI, Australian National University, Canberra, Australia
[5]Department of Geography and Environmental Sciences, Northumbria University, Newcastle, UK
[6]Center for Coastal Physical Oceanography, Old Dominion University, Norfolk, VA, USA
[7]Australian Antarctic Division, Kingston, Tasmania, Australia
[8]Australian Antarctic Program Partnership (AAPP), Institute for Marine and Antarctic Studies, and the Australian Centre for Excellence in Antarctic Science (ACEAS), both at the University of Tasmania, Australia
[9]School of Geosciences, University of Edinburgh, Edinburgh, UK
[10]School of the Environment, The University of Queensland, St Lucia, QLD, Australia.
[11]NOAA/Geophysical Fluid Dynamics Laboratory, Princeton, NJ, USA
[12]Norwegian Polar Institute, Fram Centre, Tromsø, Norway
[13]Environmental Fluid Dynamics Laboratory, New York University, NY, USA
[14]British Antarctic Survey, Cambridge, UK
[15]Department of Geography, Swansea University, Swansea, UK
[16]Institut des Geosciences de l'Environnement, Univ. Grenoble Alpes/CNRS/IRD/G-INP/INRAE, Grenoble, France
[17]Japan Agency for Marine-Earth Science and Technology (JAMSTEC), Yokohama, Japan
[18]Climate and Global Dynamics Laboratory, National Center for Atmospheric Research, Boulder, CO, USA
[19]Moss Landing Marine Laboratories, Sa José State University, Moss Landing, California, USA
[20]Thayer School of Engineering, Dartmouth College, Hanover, NH, USA
[21]Institute of Low Temperature Science, Hokkaido University, Sapporo, Japan
[22]National Centre for Atmospheric Science, Department of Meteorology, University of Reading, Reading, UK
[23]Alfred-Wegener-Institut für Polar- und Meeresforschung, Bremerhaven, Germany
[24]Akvaplan-niva AS, 9296, Tromsø, Norway

Correspondence: Claire K. Yung (claire.yung@anu.edu.au)

Abstract. Ocean-driven basal melting of Antarctic ice shelves plays an important role in the mass loss of the Antarctic Ice Sheet. Ice shelf cavity-resolving ocean models are a valuable tool for understanding ice shelf-ocean interactions and for simulating projections of ice shelf and ocean states under future climate. Designed to assess the current state of ice shelf–ocean modelling, the second Ice Shelf–Ocean Model Intercomparison Project, ISOMIP+, consists of 12 ocean model configurations submitted with a common, idealised experimental setup. Here, we focus on the experiments Ocean0–2 (Asay-Davis et

https://doi.org/10.5194/egusphere-2025-1942
Preprint. Discussion started: 24 June 2025

al., 2016), which are ocean models with idealised, static ice shelf geometries, but where the ocean reaches a balance with prescribed far-field ocean conditions. Different coefficient values are used for each model in the melting parameterisation to achieve a common, tuned melt rate since the models cover a range of types of vertical coordinates, ice–ocean boundary layer treatments, and numerical schemes. These model differences lead to spread in the resultant ocean properties, circulation, boundary-layer structure and spatial distribution of melting. We also highlight similarities between models, such as a shared linear relationship across most models between melt rate and overturning and barotropic streamfunctions, demonstrating a robust relationship between melt and circulation across models and forcing conditions. The ISOMIP+ results provide a systematic comparison of ice shelf cavity-capable ocean models. However, we also demonstrate the need for realistic ice shelf–ocean model intercomparison projects (some already underway) to assess model biases and inter-model variation against sparse observations. Further research is needed to understand the differences between models and further improve our modelled representations of the ice–ocean boundary layer and ice shelf cavity circulation.

1 Introduction

The projection of ice sheet behaviour is paramount for understanding, mitigating, and adapting to the impacts of climate change on global sea level. The Antarctic Ice Sheet, which contains most of the world's frozen freshwater, is a key driver of sea level rise over decadal and longer timescales (IPCC, 2021) and also has strong interactions with the Southern Ocean and global thermohaline circulation (e.g. Li et al., 2023) and therefore global climate. With global temperatures increasing, the sea level rise indirectly caused by the melting of ice shelves poses significant risks to coastal communities, infrastructure and ecosystems worldwide (Bronselaer et al., 2018; Sadai et al., 2022; Galton-Fenzi et al., 2025). Consequently, accurate projections of ice sheet behaviour, particularly in response to the ocean-driven basal melting of ice shelves, are crucial for informing climate policy, coastal planning, and disaster preparedness (Hinkel et al., 2019; Durand et al., 2022).

To address this challenge, numerical models have been developed to simulate the interactions between ice shelves and the ocean (e.g. Williams et al., 1998; Dinniman et al., 2016; Asay-Davis et al., 2017; Rosevear et al., 2025). These models are indispensable for understanding how ocean processes drive ice shelf melting and for projecting how ice sheets will respond to warming oceanic conditions (e.g. Holland et al., 2008; Gwyther et al., 2016; Seroussi et al., 2020; Naughten et al., 2023; Kusahara et al., 2023). However, discrepancies among different models introduce significant uncertainties in these simulations (IPCC, 2021; Naughten et al., 2018b; Seroussi et al., 2020). The first iteration of the Ice Shelf–Ocean Model Intercomparison Project (ISOMIP) was conceived in the early 2000s through the Forum for Ice Shelf Research (FRISP)[1], in response to the need for improving the accuracy and reliability of simulations by providing a standardised framework for their comparison and enhancement (Holland et al., 2003; Hunter, 2006). Through a common set of protocols and test cases for model evaluation, different models were systematically compared using highly idealised geometries and simplified physical conditions based on the original "Grosfeld" cavity (Grosfeld et al., 1997). This collaborative endeavour facilitated the identification of strengths and weaknesses of various modelling approaches and fostered model development. Although a formal ISOMIP comparison was

[1] https://scar.org/science/physical/frisp

https://doi.org/10.5194/egusphere-2025-1942
Preprint. Discussion started: 24 June 2025

not published, several studies used the protocol to demonstrate the importance of simulation of the sub-ice shelf circulation and associated numerical modelling choices for the computed melt rates in individual models (e.g. Hunter, 2006; Losch, 2008; Holland et al., 2008; Galton-Fenzi, 2009; Little et al., 2009; Gwyther et al., 2015, 2016; Mathiot et al., 2017).

Community engagement in ice sheet–ocean modelling was revitalised through the Climate and Cryosphere (CliC) project of the World Climate Research Programme (WCRP), resulting in the establishment of the Marine Ice Sheet–Ocean Model Intercomparison Project in 2014 (MISOMIP; Holland and Holland, 2015). MISOMIP sought to develop a suite of coupled glacier–ocean model benchmark tests using more complex ice and bed topography but still idealised model configurations. An ice sheet-only experiment (MISMIP+) was already under development, based on previous standalone marine ice sheet model intercomparisons (Pattyn et al., 2012, 2013). MISOMIP developed two complementary tests, an ocean-only set of simulations (ISOMIP+) and coupled ice sheet and ocean simulations (MISOMIP1), that together comprised the next-generation framework for idealised ice sheet-ocean model intercomparison (Asay-Davis et al., 2016). Building complexity on the idealised ISOMIP (Hunter, 2006) and MISMIP (Pattyn et al., 2012, 2013) frameworks, a common, high-resolution domain was used for MISMIP+, ISOMIP+ and MISOMIP1. The domain used in these experiments was designed to be representative of small-sized, laterally confined ice shelves that experience buttressing, such as Pine Island Glacier Ice Shelf, thought to be particularly vulnerable to rapid retreat and potential contributors to large amounts of sea level rise contained in the grounded ice sheet regions they buttress (Rignot et al., 2014; Favier et al., 2014; Christianson et al., 2016; Reed et al., 2024). The ISOMIP+ protocol specifies experiments testing the response to both warm and cold ice shelf cavity conditions and the transition between them. ISOMIP+ also builds on the first generation of ISOMIP by using a higher spatial resolution and a velocity-dependent basal melt parameterisation (Holland and Jenkins, 1999; Jenkins et al., 2010).

The ISOMIP+ protocol (Asay-Davis et al., 2016) has been used extensively for model comparison and development. Gwyther et al. (2020) use three ISOMIP+ models to assess the sensitivity to the vertical sampling of melt parameterisation forcing and freshwater distribution. Scott et al. (2023) and Zhou and Hattermann (2020) use the framework to verify and assess new unstructured grid ice shelf cavity ocean models and explore melt range convergence with vertical resolution and pressure gradient errors, respectively. Stern et al. (2017, 2019) use a modified ISOMIP+ setup to test a Lagrangian iceberg model. Yung et al. (in review) use two ISOMIP+ ocean models to evaluate a basal melt parameterisation incorporating the unresolved effect of stratification due to buoyant meltwater, Buissou et al. (2022) use some ISOMIP+ simulations to train and assess melt parameterisations based on neural networks, and Vaňková et al. (2025) explore relationships between melt and subglacial discharge in an ISOMIP+ model.

The related MISOMIP1 protocol has also been used for model development: Zhao et al. (2022) explore sub-ice shelf melt oscillations and the relationship with ocean circulation with the MISOMIP1 setup, whilst Favier et al. (2019) use the MISOMIP1 setup to assess basal melt parameterisations for stand-alone ice sheet models. Zhou et al. (2024) two ocean models with MISOMIP1 configurations to assess an accelerated forcing approach to coupled ice sheet–ocean modelling. Smith et al. (2021) develop the ice shelf–ocean coupling framework used in the UKESM1 climate model using the MISOMIP1 test case and assess the impact of grid resolution on coupling feedbacks. Richter et al. (in review) use the MISOMIP1 setup to develop

https://doi.org/10.5194/egusphere-2025-1942
Preprint. Discussion started: 24 June 2025

and verify a coupled ice sheet–ocean model framework. These studies demonstrate the benefit of common, idealised protocols in facilitating advances in ice shelf–ocean models.

Model developments in idealised experiments can support and ultimately transition to realistic domains for future projection simulations of Antarctic ice shelf melt (e.g. Timmermann and Hellmer, 2013; Naughten et al., 2018a; Siahaan et al., 2022; Jourdain et al., 2022; Kusahara et al., 2023; Mathiot and Jourdain, 2023; Naughten et al., 2023; Bett et al., 2024; De Rydt and Naughten, 2024) and in guiding melt parameterisations for simulations used in current and future Intergovernmental Panel on Climate Change (IPCC) reports (Jourdain et al., 2020, 2022; Burgard et al., 2022). Additionally, two realistic Antarctic ice sheet–ocean model intercomparison projects have been established since ISOMIP+, the Realistic Ice-shelf/ocean State Estimates (RISE) project focused on comparing and evaluating existing circum-Antarctic ice shelf–ocean simulations (RISE; Galton-Fenzi et al., in review) and the Marine Ice Sheet and Ocean Model Intercomparison Project – phase 2 (MISOMIP2; De Rydt et al., 2024, the next iteration of the MISOMIP collaboration), focused on the ice sheet–ocean interactions in the Weddell and Amundsen Seas.

Here, we report the results of ISOMIP+, consisting of contributions from 12 model configurations. These contributions, which include eight independent ocean models, demonstrate the increasing number of ocean models that can simulate ice shelf cavities (Dinniman et al., 2016) and the successful reach of the collaborative model intercomparison approach. After summarising the Asay-Davis et al. (2016) experimental protocol and detailing the model configurations, we present the modelled ocean properties, melt rates and drivers (friction velocity and thermal driving, used in the basal melt parameterisation) and ocean cavity circulation. While we verify the internal consistency of the basal melting parameterisation and water mass conservation, we cannot verify the idealised simulations with observations and no analytical solutions have been found. Instead, we present and compare the model results and aim to understand the causes of their similarities and differences.

2 Experimental design

The ISOMIP+ protocol, documented by Asay-Davis et al. (2016), consists of five different experiments using ocean models: a tuning experiment (Ocean0), two experiments with static ice shelves and a warming or cooling ocean boundary forcing (Ocean1 and Ocean2), and two experiments with a prescribed retreat and re-advance of the ice shelf grounding lines (Ocean3 and Ocean4). In this study, we do not describe the latter two experiments with dynamic ice shelves. Their results are provided in an analysis of a separate intercomparison for the MISOMIP1 two-way coupled ice sheet–ocean models (Seroussi et al., *in prep.*). The ISOMIP+ experiments use common geometries (topography and the ice shelf thickness), boundary and initial conditions, and mixing and melt parameterisations. In this section, we briefly summarise the protocol and refer the reader to Asay-Davis et al. (2016) for further details. This study focuses on the "common" (COM) experiments where models strictly follow the protocol and are tuned to achieve similar melt rates. Some participants also submitted "typical" (TYP) results for their models where parts of the model protocol were relaxed, described in Sect. 2.7.

https://doi.org/10.5194/egusphere-2025-1942
Preprint. Discussion started: 24 June 2025

2.1 Geometric setup

The ISOMIP+ topography and ice shelf draft (Fig. 1) are idealised geometric configurations that overlap with the MISMIP+ (Cornford et al., 2020; Asay-Davis et al., 2016) and MISOMIP1 domain. The domain has size 480 km and 80 km in the x and y directions, respectively. The x direction aligns with the direction of the ice flow, towards the calving front. This choice does not affect the ocean circulation, since the participating models use the f-plane approximation (referenced to 75°S latitude). The bed topography is the same as MISMIP+ and the ice shelf draft for Ocean0 and Ocean1 is a steady state ice shelf configuration computed with the BISICLES model (Cornford et al., 2013) with the MISMIP+ Ice1 parameters (Asay-Davis et al., 2016; Cornford et al., 2020), and computed similarly for Ocean2 with MISMIP+ Ice1r parameters. The bed topography (also provided as an analytic expression; Asay-Davis et al., 2016) and ice shelf draft were provided on a 1 km horizontal resolution grid. Participants then interpolated and smoothed the bed topography and ice shelf draft using different methods to achieve a horizontal grid resolution of 2 km (details are in Sect. 3; see Fig. S11, S12). However, where interpolation results in an ice shelf thickness less than 100 m, the thickness is set to zero to represent a steep calving front. The BISICLES geometry also prescribes a steep calving front located at $x = 640$ km. Models are configured with 36 vertical levels, spread over the 720 m maximum depth in different ways depending on the vertical coordinate used, resulting in varying vertical resolution beneath the ice shelf. All z-level models use a vertical grid size of 20 m with differing partial cell choices. In the Ocean0-2 experiments discussed in this paper, the ice shelf draft is fixed and does not change in time.

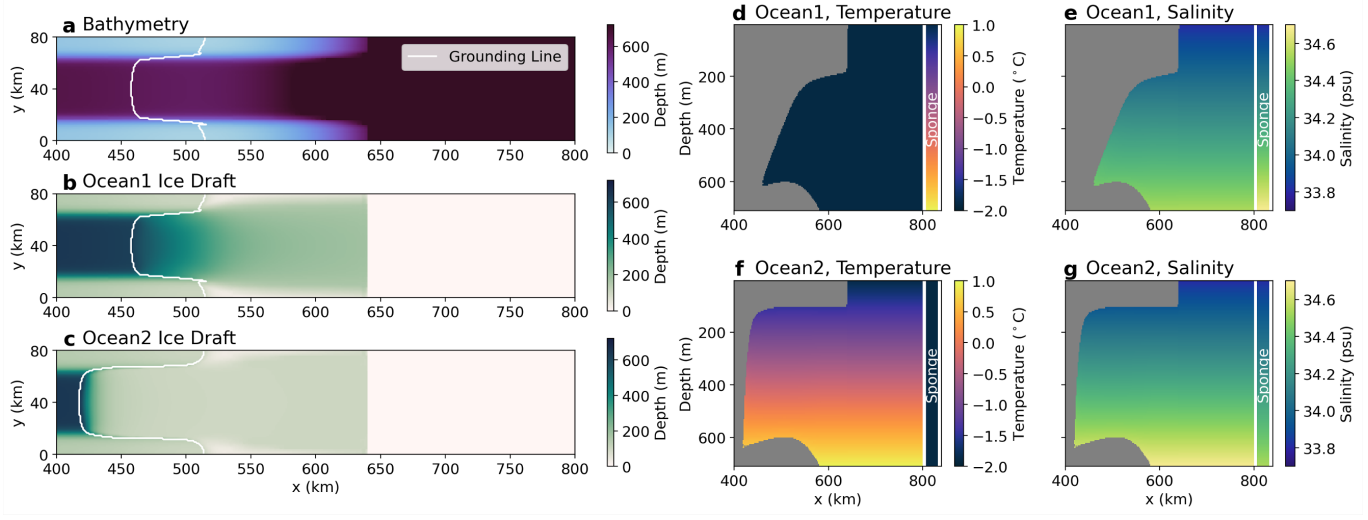

Figure 1. Experiment geometry and initial conditions, showing the bathymetry (a), and ice shelf draft for the Ocean0 and Ocean1 (b) and Ocean2 (c) experiments, and cross sections of the temperature and salinity initial conditions for Ocean1 ("cold", d,e) and Ocean2 ("warm" f,g). The sponge forcing applied at the positive x boundary is the opposite (cold/warm) of the initial conditions. Ocean0 uses the warm initial conditions and warm sponge boundary.

https://doi.org/10.5194/egusphere-2025-1942
Preprint. Discussion started: 24 June 2025

2.2 Initial and boundary conditions

The initial conditions for the experiments are either a "warm" or "cold" profile (Fig. 1d–g). Potential temperature (referred to as temperature in the remainder of this manuscript) and practical salinity (noting that we use the PSS-78 salinity scale, so values do not have units) vary uniformly with depth. For the cold profile (qualitatively representative of the Ross or Weddell Seas), the temperature is a constant -1.9°C and salinity varies linearly between 33.8 at the surface (0 m depth) to 34.55 at the bottom (720 m). For the warm profile (qualitatively representative of the Amundsen and Bellingshausen Seas, with warm, salty Circumpolar Deep Water intrusions at depth, e.g., Dutrieux et al., 2014), the temperature and salinity varies from -1.9°C and 33.8 at the surface to +1°C and 34.7 at the seafloor. By making use of the experiment's linear equation of state, the cold and warm profiles are designed to have the same density profile (Fig. 6 from Asay-Davis et al., 2016). In all experiments, the ocean begins at rest.

The boundaries on all side walls use no-slip conditions whilst top and bottom boundaries employ a quadratic drag with drag coefficient C_D. Additionally, the temperature and salinity are forced using a restoring sponge at the "northern" x boundary. This sponge is applied over the entire ocean depth and y direction, and linearly increases in restoring strength from no restoring at $x = 790$ km to full restoring at $x = 800$ km, with a restoring timescale of 0.1 days (i.e. 2.4 hours) towards either the warm or cold profile. Sea level may also be restored if melting is implemented as a volume flux using surface mass fluxes in the sponge layer; otherwise, there are no open ocean surface fluxes (unless specified in Section 3).

2.3 Equation of state

The experiment protocol prescribes a linear equation of state given by

$$\rho = \rho_{\text{ref}} \left[1 - \alpha(T - T_{\text{ref}}) + \beta(S - S_{\text{ref}})\right] , \tag{1}$$

where the reference density, temperature and salinity are ρ_{ref}, T_{ref} and S_{ref}, and the thermal expansion and haline contraction coefficients are α and β. Numerical values are presented in Table 1.

2.4 Melt parameterisation

Ice shelf basal melt rates are calculated using the three-equation parameterisation (Hellmer and Olbers, 1989; Holland and Jenkins, 1999) with a linear dependence of the freezing temperature on pressure and salinity and constant transfer coefficients (Jenkins et al., 2010):

$$T_{z_d} = \lambda_1 S_{z_d} + \lambda_2 + \lambda_3 p_{z_d} \tag{2}$$

$$\rho_{\text{fw}} m_w L = -\rho_{\text{sw}} c_w u_* \Gamma_T (T_{z_d} - T_w) \tag{3}$$

$$\rho_{\text{fw}} m_w S_{z_d} = -\rho_{\text{sw}} u_* \Gamma_S (S_{z_d} - S_w) \tag{4}$$

$$u_*^2 = C_D \left(u_w^2 + u_{\text{tidal}}^2\right) . \tag{5}$$

https://doi.org/10.5194/egusphere-2025-1942
Preprint. Discussion started: 24 June 2025

Table 1. Parameters for the ISOMIP+ common experiments, reproduced from Asay-Davis et al. (2016)

Parameter	Value	Description
$\Delta x = \Delta y$	2 km	Horizontal grid spacing
c_w	3974 J °C^{-1} kg^{-1}	Specific heat capacity of seawater
L	3.34×10^5 J kg^{-1}	Latent heat of fusion of ice
λ_1	-0.0573 °C	Liquidus slope (salinity dependence)
λ_2	0.0832 °C	Liquidus intercept
λ_3	-7.53 ×10^{-8} °C Pa^{-1}	Liquidus pressure coefficient
Γ_T	model specific	Non-dimensional heat transfer coefficient
Γ_S	$\Gamma_T/35$	Non-dimensional salt transfer coefficient
$C_{D,\text{top}}$	2.5×10^{-3}	Top drag coefficient
$C_{D,\text{bottom}}$	2.5×10^{-3}	Bottom drag coefficient
u_{tidal}	0.01 m s^{-1}	Root Mean Square velocity associated with tides
κ_i	0	Heat diffusivity into ice (perfectly insulating)
ν_{unstab}	0.1 m^2 s^{-1}	Convective vertical viscosity
κ_{unstab}	0.1 m^2 s^{-1}	Convective vertical diffusivity
ν_{stab}	1×10^{-3} m^2 s^{-1}	Stable vertical eddy viscosity
κ_{stab}	5×10^{-5} m^2 s^{-1}	Stable vertical eddy diffusivity
ν_H	6.0 m^2 s^{-1}	Horizontal eddy viscosity
κ_H	1.0 m^2 s^{-1}	Horizontal eddy diffusivity
ρ_{fw}	1000 kg m^{-3}	Density of fresh water
ρ_{sw}	1028 kg m^{-3}	Reference density of seawater
T_{ref}	-1 °C	Reference potential temperature for linear equation of state (EOS)
S_{ref}	34.2	Reference salinity for linear EOS
ρ_{ref}	1027.51 kg m^{-3}	In situ density for linear EOS
α_{lin}	3.733×10^{-5} °C^{-1}	Thermal expansion coefficient for linear EOS
β_{lin}	7.843 ×10^{-4}	Salinity contraction coefficient for linear EOS

https://doi.org/10.5194/egusphere-2025-1942
Preprint. Discussion started: 24 June 2025

All parameters are described in Table 1. Here, the liquidus slope is λ_1, intercept λ_2 and pressure coefficient λ_3. The melt rate m_w is expressed as a freshwater flow rate ($\mathrm{m\,s^{-1}}$), which is solved by the equations along with the temperature and salinity at the ice–ocean interface T_{z_d} and S_{z_d}. The temperature T_w, salinity S_w and velocity u_w represent the ocean properties outside of the turbulent ice-ocean boundary layer and can be determined by models in different ways, but are generally taken as the surface mixed layer properties or properties averaged over a constant distance from the ice. Salt and freshwater densities are ρ_{sw} and ρ_{fw}. The latent heat of fusion is L and the specific heat capacity of water is c_w. The drag coefficient C_D for determining the friction velocity is the same as the dynamic drag boundary condition at the top and bottom boundaries.

Here, the prescribed tidal velocity u_{tidal} is used to account for the additional ocean motion (ostensibly due to tides) in the friction velocity (u_*). Without this prescribed velocity, no melt would occur when the ocean is at rest, even when heat is available for melting, contradicting our expectations from both theory and observations. It is worth noting that there are more complex and accurate methods to include the effect of tidal motion (Jourdain et al., 2019). The transfer coefficients Γ_T and $\Gamma_S = \Gamma_T/35$ are tuned constants (see Sect. 2.6). Using constant transfer coefficients is an approximation that does not hold in the real world, and models may use variable transfer coefficients (e.g. Holland and Jenkins, 1999). Furthermore, the ice is considered to be perfectly insulating without any conductive heat flux at the ice–ocean interface. For a review on melt parameterisations in ice shelf–ocean models, see Malyarenko et al. (2020) and Rosevear et al. (2025).

Gwyther et al. (2020) demonstrate with the ISOMIP+ setup that melt rates are impacted by both the distance across which the ocean properties $<>_w$ are sampled and the distance across which the meltwater is distributed. The ISOMIP+ model contributions vary in their sampling and distribution methods; these are described in Sect. 3. Additionally, models vary in their addition of freshwater, either as a volume or virtual salt flux (Table 2).

2.5 Mixing parameterisation

The mixing of momentum and tracers in vertical and horizontal directions is parameterised using a Laplacian (harmonic) operator with constant coefficients (values are prescribed in Table 1). Vertical (or more precisely, between model layers) diffusivity is κ_{stab}, except when there is locally unstable stratification, where it increases account for convective instability (to κ_{unstab}) or using a model-dependent convective adjustment scheme described in Sect. 3. Similarly, the vertical viscosity ν_{stab} in the interior also increases with unstable local stratification to ν_{unstab}. Horizontal diffusivity and viscosity are κ_H and ν_H, respectively, though numerical mixing may also be significant. Mixing also occurs implicitly via the distribution of meltwater: typically, z-coordinate models use a Losch (2008)-style scheme where meltwater is distributed evenly over a fixed distance from the ice. This distance is usually the z-coordinate thickness, which usually covers multiple grid cells if partial cells are used. Other models may distribute meltwater only in the uppermost cell, thereby removing the implicit mixing due to meltwater distribution (details in Sect. 3).

2.6 Experiments Ocean0, Ocean1 and Ocean2

The Ocean0 tuning experiment uses the warm initial conditions and warm northern boundary sponge forcing with the ice draft of Fig. 1b. This allows a quasi-equilibrium, warm-shelf melt rate and circulation to be attained quickly. For the COM

https://doi.org/10.5194/egusphere-2025-1942
Preprint. Discussion started: 24 June 2025

experiments, participants were requested to modify Γ_T and $\Gamma_S = \Gamma_T/35$ to achieve a target area-averaged melt rate at depth ($z < -300$ m) of 30 ± 2 m yr^{-1}. This tuning involved running multiple Ocean0 configurations to sample various $\Gamma_{T,S}$ until the target melt rate was achieved, with larger $\Gamma_{T,S}$ producing more melt via Eqns. 3–4. The Ocean0 simulations use these optimal transfer coefficients and were run for 1 year, or longer if quasi-equilibrium was not achieved within 6 months.

Ocean1 and Ocean2 use the same optimally tuned transfer coefficients as Ocean0 but with different restoring forcing, initial conditions and/or ice draft. Ocean1 begins with cold initial conditions but a warm restoring boundary (Fig. 1d) and same ice draft as Ocean0 (Fig. 1b), whereas Ocean2 begins with warm initial conditions and a cold restoring boundary (Fig. 1f) and a different ice draft (Fig. 1c), consisting of a steeper ice base slope over a narrower x-axis extent compared to Ocean1. Both experiments are run for 20 years to investigate the timescales and states during the transition between warm and cold states of an ice shelf cavity.

2.7 Typical experiments

In their typical usage (for both realistic and idealised simulations), ice shelf–ocean model configurations generally differ from the prescribed ISOMIP+ protocol. For example, they may employ different mixing schemes, horizontal resolutions, or ice shelf melt parameterisations (e.g. Holland and Jenkins, 1999). The typical "TYP" simulations submitted by participants use the same geometry and boundary conditions as the Ocean0–2 COM experiments but with other parameters, resolutions, or physics schemes configured per participant choices for more conventional use, with these settings often taken from previous simulations. Since ice shelf melt parameterisations may have been modified, most TYP experiments do not use a tuned transfer coefficient to achieve the COM Ocean0 target melt rate. The TYP experiments provide an additional measure of variability between models, which are compared in Sect. 4.5. Any differences between models' TYP and COM configurations are described in Appendix A. Since participants were asked to prioritise COM simulations, not all participants submitted TYP experiments (Table 2).

3 Model descriptions

Twelve different model configurations (eight independent models) were submitted to ISOMIP+ with results for the Ocean0-2 experiments. Table 2 summarises these model configurations. All model configurations solve the primitive equations under hydrostatic and Boussinesq approximations. The details of each model and any deviations from the COM protocol of Sect. 2 are described here.

The ISOMIP+ model results were submitted between 2016 and 2020. Many model codes have evolved and improved since their original submission, and erroneous model behaviour may reflect the imperfect application of the idealised experiment protocol, which differed from the typical, realistic use cases for many models. Additionally, a multi-model mean of these model results may not be the "correct" solution to the ISOMIP+ experimental setup; we cannot verify the simulations with observations, and no analytical solutions have been found. We analyse the original ISOMIP+ submissions with these caveats and aim to understand the causes of similarities and differences between models.

https://doi.org/10.5194/egusphere-2025-1942
Preprint. Discussion started: 24 June 2025

Table 2. Summary of the model configuration submissions for the ISOMIP+ Ocean0, Ocean1 and Ocean2 experiments. We list the vertical coordinate (z-level, sigma/terrain-following (s-level), isopycnal, and z/s ALE for Arbitrary Eulerian-Lagrangian coordinates with a quasi z–ice shelf-following target coordinate), heat transfer coefficient for COM experiments, meltwater addition method and whether TYP Ocean1 and Ocean2 experiments were also submitted. The method of meltwater addition is either a virtual salt flux or volume flux. In the case of a volume flux, we also specify whether the sea level is constrained to be constant via an adjustment applied to the entire open ocean, applied to just the sponge boundary, or not constrained ("none"). COM salt transfer coefficients were fixed according to $\Gamma_S = \Gamma_T / 35$.

Model configuration (submitter)	Vertical coordinate	COM heat transfer coefficient Γ_T	Meltwater addition (sea level method)	TYP submission
COCO (Kusahara)	z-level	0.025	volume flux (open ocean)	
FVCOM (Zhou)	s-level	0.2	virtual salt flux	✓
MITgcm-BAS (Jordan)	z-level	0.011 / 0.036*	virtual salt flux	
MITgcm-BAS-Coupled (Jordan)	z-level	0.0135**	virtual salt flux	
MITgcm-JPL (Nakayama)	z-level	0.0325	virtual salt flux	
MOM6-SIGMA-ZSTAR (Marques)	z/s ALE	0.045	volume flux (sponge)	
MOM6-LAYER (Marques)	isopycnal	0.1423	volume flux (none)	✓
MPAS-Ocean (Asay-Davis)	z/s ALE	0.0194	volume flux (sponge)	✓
NEMO-CNRS (Jourdain)	z-level	0.026	volume flux (open ocean)	✓
NEMO-UKESM1is (Smith)	z-level	0.045	volume flux (open ocean)	✓
POP2x (Asay-Davis)	z-level	0.1146	virtual salt flux	✓
ROMS (Gwyther)	s-level	0.05	virtual salt flux	✓

*Derived transfer coefficient for Ocean1 simulation is 0.011 and 0.036 for Ocean2, see Sect. 3.3 for more details. **Using derived transfer coefficient rather than reported value (Sect. 3.3)

3.1 COCO

One submission is based on COCO version 4.9 (Hasumi, 2006), using the ice shelf component described in Kusahara and Hasumi (2013). The horizontal direction uses an Arakawa B-Grid. The vertical direction employs a hybrid coordinate system consisting of sigma layers in the near-surface and z-coordinate layers below. The ice shelf component is only activated in the z-coordinate layers. The configuration uses a second-order centred scheme for momentum advection and the UTOPIA/QUICKEST scheme for horizontal and vertical tracer advection (Leonard, 1979; Leonard et al., 1993, 1995). The melt rate is calculated by sampling the temperature, salinity, and velocity in the uppermost grid cell under the ice shelf. Meltwater is also distributed on the uppermost grid cell under the ice shelf. The mean sea level is maintained by removing the mean sea level anomaly in the open water area at each time step. The land mask is generated by designating areas where the water column thickness is less than 40 m (i.e. 2-grid cells) as land grid points. The ice draft is also manually filled in at the sides to create a smoother geometry (e.g. Fig. 4, S11, S12). The COCO submission uses partial cells to better represent the bottom topography in the z-coordinate model (Adcroft et al., 1997), with an accuracy of 10% of the grid cell thickness (i.e. 2 m). For the ice shelf draft, a full step representation is used to reduce grid size noise in the velocity field.

https://doi.org/10.5194/egusphere-2025-1942
Preprint. Discussion started: 24 June 2025

3.2 FVCOM

One submission uses the version of the unstructured grid Finite Volume Community Ocean Model (FVCOM) that resolves ice shelf cavities (Chen et al., 2003; Zhou and Hattermann, 2020). FVCOM solves the governing equations in integral form by computing fluxes between non-overlapping horizontal triangular control volumes using generalized terrain-following coordinates. In the COM submission, the model setup uses a horizontal grid mesh composed of equilateral triangles of sidelength 2 km, and 35 terrain-following vertical layers with slightly increasing resolution towards the bottom. Both momentum and tracers are advected using a second-order upwind scheme. For the vertical advection of tracers, the second-order Multidimensional Positive Definite Advection Transport Algorithm is used (Smolarkiewicz and Szmelter, 2005). To address unstable vertical mixing, salinity and temperature values in the two layers are averaged if the upper layer's density is greater than that of the lower layer. The melt rate is calculated by sampling the temperature, salinity, and velocity in the uppermost grid cell under the ice shelf. The ice draft topography is linearly smoothed within 20 km of the ice front (Fig. 2b). The minimum water column thickness is 30 m. In addition, the bathymetry in Ocean2 (seen in Fig. 3b) is further adjusted according to the water column thickness output from the ROMS model, which was first smoothed using a mean filter over a square of size 10 km side length. It was not possible to reach the target melt rate of $30 \pm 2\,\mathrm{m\,yr^{-1}}$ below 300 m depth in FVCOM during the tuning stage in Ocean0. Instead, the large value of $\Gamma_T = 0.2$ chosen resulted in an equilibrium melt rate of $18.9\,\mathrm{m\,yr^{-1}}$ in Ocean0.

3.3 MITgcm

Three submissions are based on the Massachusetts Institute of Technology general circulation model (MITgcm; Marshall et al., 1997), from Jet Propulsion Laboratory (hereafter MITgcm-JPL), the British Antarctic Survey (MITgcm-BAS) and a second configuration from the British Antarctic Survey that uses the coupled ice–ocean framework as described in Jordan et al. (2018) (MITgcm-BAS-Coupled). The implementation of ice shelf cavities in MITgcm is described in Losch (2008). MITgcm is a finite volume model. The configurations used here employ an Arakawa C-grid and a z-level vertical coordinate. Momentum is advected using a second-order centered scheme, while tracers are advected using a third-order Direct Space-Time (DST) flux limiter scheme (note this scheme was later found to cause some spurious behaviour, see Sect. 4.4). Differing from the COM protocol, unstable vertical mixing is parameterised with the convection scheme of Cessi and Young (1996), which instantaneously mixes the unstable density gradients, and is applied every time step. The melt rate is calculated by sampling the temperature, salinity, and velocity within a fixed 20 m boundary layer beneath the ice. Melt fluxes are also distributed over a 20 m layer beneath the ice.

The major difference between the three MITgcm COM submissions is the choice of heat and salt transfer coefficients at the ice–ocean interface (Table 2), the minimum water column thickness and the limit on the size of partial grid cells at the ice–ocean boundary. MITgcm-BAS uses a minimum water column thickness of 40 m, which is maintained by excavating the ice draft while keeping the bottom topography and grounding line fixed. MITgcm-BAS-Coupled imposes a minimum water column thickness of 0.5 m. The minimum size of partial cells is 25% of a regular cell for MITgcm-JPL and 20% for MITgcm-BAS and MITgcm-BAS-Coupled. All three configurations achieved similar, but not identical, melt rates at depth during the tuning

https://doi.org/10.5194/egusphere-2025-1942
Preprint. Discussion started: 24 June 2025

experiment that fell within the target error margin, explained by their use of similar but not equal heat transfer coefficients and partial cell limits. The MITgcm-BAS-Coupled setup requires the use of a small (of the order of 0.05 m) minimum water column under all grounded ice in the domain (seen in Fig. 2d) to represent grounding-line retreat when used in coupled mode (Goldberg et al., 2018).

Heat transfer coefficients Γ_T for MITgcm-BAS and MITgcm-BAS-Coupled were initially reported as 0.019 and 0.021 respectively. However, subsequent analyses verifying the melt parameterisation (Sect. 4.4) revealed inconsistencies between the quoted transfer coefficients and the model output. These analyses suggested that MITgcm-BAS-Coupled used a transfer coefficient of 0.0135, and MITgcm-BAS used 0.011 in the Ocean1 experiment and 0.036 in the Ocean2 experiment (Table 2). Due to a lack of model data traceability during the intervening years, we are unable to verify which transfer coefficients these experiments used. It is hence possible that the experimental protocol was not completely followed, particularly for the MITgcm-BAS Ocean2 experiment (in the MITgcm-BAS Ocean1 experiment we can verify it achieved the tuned melt rate of $30\,\mathrm{m\,yr^{-1}}$ averaged below 300 m depth at steady state, see Sect. 4.5). For MITgcm-BAS-Coupled we are reasonably confident that the value 0.0135 was used because we have found ISOMIP+ Ocean3 and Ocean4 simulations using that value.

3.4 MOM6

Two submissions are based on the Modular Ocean Model version 6 (MOM6; Adcroft et al., 2019). MOM6 is a finite volume model, uses the Arakawa C-grid and is formulated in a generalised vertical coordinate form. Momentum is advected using a second-order centred scheme, while tracers are advected using a piecewise linear method. Vertical mixing due to shear instabilities and convection is represented using the Jackson et al. (2008) scheme, with the critical Richardson number set to 0.25. The minimum vertical viscosity within the surface boundary layer is $10^{-2}\,\mathrm{m^2\,s^{-1}}$. Melting is set to zero when the total water column thickness is less than 10 m, and meltwater is added as a volume flux. The differences between the two MOM6 COM submissions are described below.

3.4.1 MOM6-SIGMA-ZSTAR

For the MOM6-SIGMA-ZSTAR configuration, the vertical coordinate is a hybrid between terrain-following (in the cavity) and z^* coordinates (in the open ocean) (Stern et al., 2017, 2019). Vertical mixing at the surface boundary layer in MOM6-SIGMA-ZSTAR is parameterised with an energetically consistent planetary boundary layer scheme (Reichl and Hallberg, 2018). The temperature, salinity and velocity used in the melt parameterisation are averaged within 20 m of the ice draft; the velocity is further averaged to the tracer grid points using the four horizontal neighbours. Sea level is maintained by adding a mass flux in the restoring region (while ensuring no change to buoyancy forcing). The ice draft topography is smoothed using a Gaussian filter with a half-width of 2 km.

https://doi.org/10.5194/egusphere-2025-1942
Preprint. Discussion started: 24 June 2025

3.4.2 MOM6-LAYER

For the MOM6-LAYER configuration, the vertical coordinate is isopycnal. Vertical mixing at the surface boundary layer in MOM6-LAYER uses the bulk mixed layer scheme described in Hallberg (2003), with a minimum boundary layer thickness of 10 m. MOM6-LAYER does not use a sea level correction, so sea level increases throughout the experiment, resulting in a minor long-term drift in the melt rate of the experiments (more prominent in Ocean1) as the ocean temperature at the ice base depth is modified. The temperature, salinity and velocity used in the melt parameterisation are averaged within 10 m of the ice draft; the velocity is further averaged to the tracer grid points using the four horizontal neighbours. Meltwater is distributed into the upper layer of the bulk mixed layer. The ice draft topography is smoothed using a Gaussian filter with a half-width of 5 km in the x-direction and 1 km in the y-direction. The ice thickness near the grounding line is decreased to maintain a minimum water column thickness of 40 m. The calving criterion (removing ice thinner than 100 m) is not applied near the ice front to minimise pressure gradient errors.

3.5 MPAS-Ocean

One submission uses the Model for Prediction Across Scales Ocean (MPAS-Ocean; Ringler et al., 2013; Petersen et al., 2018) version 6.1. MPAS-Ocean uses finite volume methods on an Arakawa C-grid. The configuration has an Arbitrary Lagrangian-Eulerian (ALE) vertical coordinate, which smoothly transitions from z^* (Adcroft and Campin, 2004) in the open ocean (with 36 vertical layers of 20 m resolution) to a terrain-following top coordinate under ice shelves. The coordinate under ice shelves constrains layer thicknesses such that the local Haney number (rx1; Haney, 1991) does not exceed a maximum value of 5. This prevents large horizontal pressure gradient errors due to the tilted vertical coordinate. Momentum is advected using a second-order, kinetic-energy-conserving scheme (Ringler et al., 2010) and tracers are advected with a third-order, flux-corrected transport (FCT) scheme (Skamarock and Gassmann, 2011). MPAS-Ocean's melt parameterisation uses temperature and salinity that are averaged within 10 m of the ice draft. The far-field ocean speed $|u_w| = \sqrt{2E_K}$ is computed from kinetic energy E_K at cell centres in the layer closest to the interface, and is not averaged vertically over multiple layers. Melt fluxes (heat and freshwater) are distributed based on an exponentially decaying transmission function $T = e^{-(z-z_d)/D}$, where z_d is the ice draft and the length scale of decay $D = 10$ m. Sea level is approximately maintained, for all but the Ocean0 experiment, using negative freshwater fluxes applied in the northern restoring region. The fluxes are adjusted each month to match the freshwater flux from melting averaged over the previous 3 months. The provided ISOMIP+ topography was modified by smoothing with a Gaussian filter with a half-width of 2 km before interpolating to the 2 km grid. A minimum thickness of 3 layers was maintained by deepening bathymetry near the grounding line.

3.6 NEMO

Two submissions are based on NEMO, the Nucleus for European Modelling of the Ocean (Madec et al., 2019): a version used at the French National Centre for Scientific Research (CNRS) (e.g., Jourdain et al., 2017) and a version used in the UK Earth System Model (UKESM, Smith et al., 2021). The NEMO-CNRS configuration is based on a post-v3.6 release of

https://doi.org/10.5194/egusphere-2025-1942
Preprint. Discussion started: 24 June 2025

NEMO that is described as the "COM" configuration in Favier et al. (2019), with details on the model parameters in Jourdain (2019). The NEMO-UKESM1is configuration is the "GO7" version described in Storkey et al. (2018). Both configurations use finite-difference methods on an Arakawa C-grid (Arakawa, 1966). A z^* coordinate (Campin et al., 2008) is used with a nominal uniform vertical resolution of 20 m. For a better representation of the topography, partial cells are used in the lowest and uppermost grid cells (Barnier et al., 2006; Mathiot et al., 2017). NEMO-CNRS makes use of the third-order Upstream Biased Scheme (UBS) scheme for momentum advection (flux form) and for horizontal tracer advection (Madec et al., 2019), and a second-order flux corrected transport scheme is used for vertical tracer advection. In NEMO-UKESM1is, momentum is advected in a vector invariant form, and tracers are advected with a Lax-Wendroff Total Variance Dissipation (TVD) scheme. Vertical mixing in NEMO-CNRS follows the ISOMIP+ protocol, while NEMO-UKESM1is uses a different "TKE scheme" (Madec et al., 2019), in which the background viscosity is set to the recommended stable vertical eddy viscosity and diffusivity (Table 1), with double diffusion mixing for tracers. The melt rates are calculated using temperature, salinity and velocity averaged over the top 20 m of the water column. The ice shelf meltwater and associated heat are also vertically spread over the top 20 m. To maintain the mean sea level, ice shelf melting in NEMO-CNRS is compensated by a uniform water flux correction applied at the open ocean surface at each time step, with no associated latent heat and salt flux as described in equations 34–36 of Asay-Davis et al. (2016). In NEMO-UKESM1is, this correction was incorrectly allowed to affect the salinity of the remaining surface water. For cases of significant ice shelf melting, this issue leads to salinification of the open ocean surface and unwanted convective mixing, cooling the interior of the domain (e.g. Fig. 2j). As NEMO needs at least two vertical cells to resolve a water column, the topography is adjusted by "digging" into the ice in NEMO-UKESM1is, and equally into the ice and the bottom topography in NEMO-CNRS. Water columns of only one grid cell width in either zonal or meridional directions are also removed.

3.7 POP2x

One submission uses the Parallel Ocean Program 2 eXtended (POP2x), a version of POP2 that includes ice shelf cavities (Smith et al., 2010). POP2x uses finite-difference methods on an Arakawa B-grid. It has a z-level vertical coordinate with 20 m vertical resolution and partial top and bottom cells to represent the topography with higher fidelity. Momentum is advected using a second-order, centred scheme and tracers are advected with a flux-limited Lax-Wendroff scheme (Lax and Wendroff, 1960). POP2x's melt parameterisation uses far-field temperature and salinity, averaged over the top 20 m - from the top of the first partial cell down to the remaining required fraction of the second vertical layer. The far-field ocean velocity used in the melt parameterisation is averaged over the four neighbouring B-grid points only in the upper vertical layer. Melt fluxes (heat and freshwater) are distributed over the upper 20 m. After interpolation and removing ice thinner than 100 m, the topography is modified by (1) smoothing with a Gaussian filter with half-width of 2 km, (2) deepening bathymetry near the grounding line to maintain a minimum water column thickness of 40 m, (3) either thickening or removing partial top cells thinner than 5 m, and (4) adjusting the ice draft and bathymetry to ensure horizontal connectivity between neighbouring cells.

https://doi.org/10.5194/egusphere-2025-1942
Preprint. Discussion started: 24 June 2025

3.8 ROMS

One submission is based on the Regional Ocean Modeling System (ROMS; Shchepetkin and McWilliams, 2009), adapted to include ice shelf cavities (Dinniman et al., 2007; Galton-Fenzi et al., 2012). ROMS is a finite volume model that uses an Arakawa C-grid and a terrain-following vertical coordinate system. Only 21 vertical layers are used in the ROMS configuration, with a higher resolution near the surface and bottom. The mean top layer thickness is 0.5 m near the grounding line, 3 m at the mid-ice shelf, and 5 m near the ice front. Momentum is advected using a 3rd order upstream scheme (fourth-order centred for the barotropic momentum), and all tracers are advected using a third-order upstream scheme in the horizontal direction and a fourth-order centred scheme in the vertical. Horizontal mixing is along geopotential (i.e. horizontal, not the model terrain following) surfaces. Basal melting and freezing are computed using temperature, salinity and velocity from the top vertical layer. Heat and meltwater fluxes are distributed at the surface of the top layer only. The topography was smoothed with a 4th-order Shapiro filter to lower the maximum "slope parameter" (Beckmann and Haidvogel, 2003) to 0.1. A minimum water column depth of 20 m is used. It was not possible to reach the target melt rate of $30 \pm 2\,\mathrm{m\,yr^{-1}}$ below 300 m depth in ROMS during the tuning stage in Ocean0. Instead, the chosen value of Γ_T = 0.05 results in an equilibrium melt rate of $14\,\mathrm{m\,yr^{-1}}$.

4 Results

Here, we present the ISOMIP+ results, beginning with steady state transect profiles, melt and circulation (Sects. 4.1, 4.2), then exploring the transient response (Sect. 4.3), differences and drivers of melt between models (Sect. 4.4) and an alternative set of experiments where parts of the experimental protocol were relaxed (Sect. 4.5).

4.1 Steady state temperature profiles and melt rate patterns

In this section, we present the steady state temperature profiles and melt rate spatial distributions at the end of the Ocean1 and Ocean2 COM experiments. We take results from the average of the final year (year 20). By then, Ocean1 melt rates are approximately constant, but Ocean2 is still evolving (see Sect. 4.3 for further details).

Temperature and salinity distributions at year 20 of the Ocean1 and Ocean2 COM simulations at the y = 40 km transect show similarities between models (Figs. 2, 3 for temperature and Figs. S7, S8 for salinity). Though Ocean1 is initialised with cold conditions, the stratification inside the cavity resembles the warm restoring conditions at the end of the simulation, with an additional cold boundary layer near the ice. Similarly, Ocean2, which is initialised with warm conditions, ends up resembling the cold restoring conditions. However, there are differences between the models; in Ocean1, NEMO-UKESM1is has a relatively colder interior (Fig. 2j), and POP2x has a colder boundary layer (Fig. 2k, see also Fig. 13k) than most other models. The cold interior of NEMO-UKESM1is can be explained by spurious convection arising from the incorrect water flux correction, as discussed in Sect. 3.6. In Ocean2, temperatures are more uniform within the domain, matching the uniform -1.9 °C sponge forcing, but MITgcm-BAS-Coupled, MITgcm-JPL and NEMO-CNRS have a warmer interior of the cavity with temperatures reaching -1.6°C. This warm interior may be associated with remnant warm water from the Ocean2 warm

https://doi.org/10.5194/egusphere-2025-1942
Preprint. Discussion started: 24 June 2025

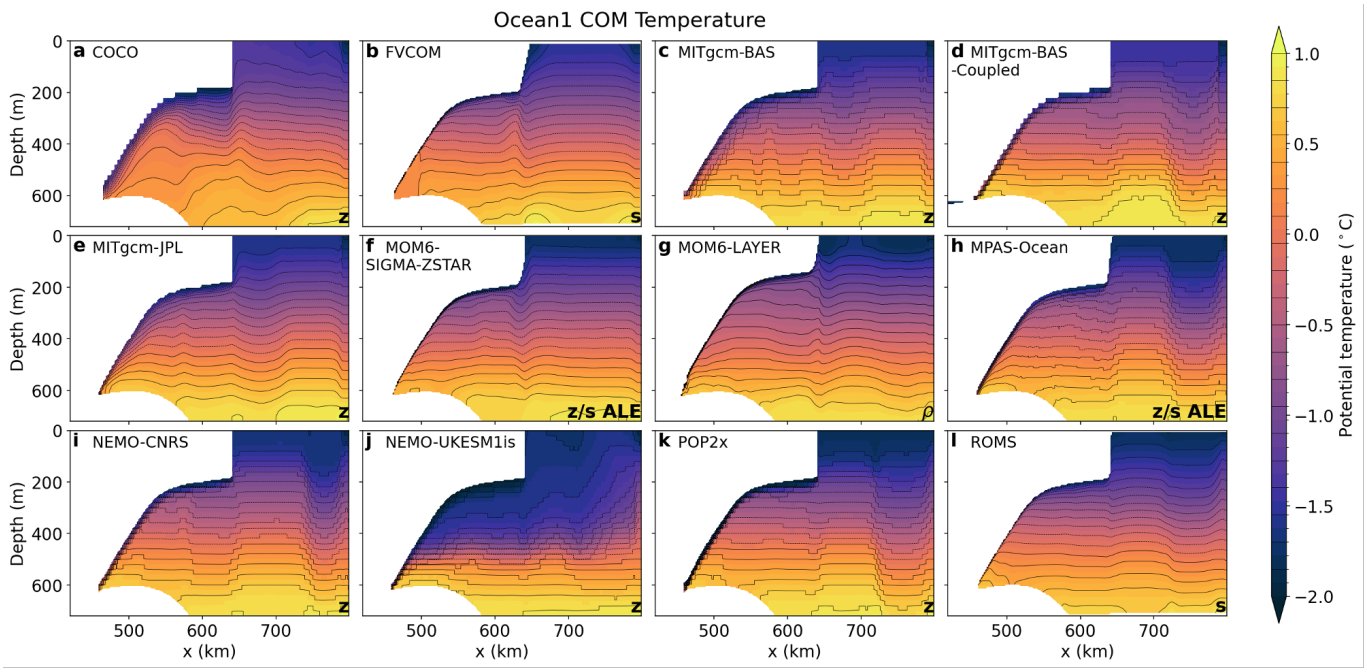

Figure 2. Steady state (average of year 20) temperature transect along $y = 40$ km in the Ocean1 COM experiment. Model vertical coordinates are labelled in the lower right corner, with z for z-coordinate models, s for terrain-following, ρ for isopycnal, and z/s ALE for Arbitrary Lagrangian-Eulerian coordinates with a quasi z–ice shelf-following target coordinate (Table 2).

initial conditions that have not been circulated out of the domain by the boundary forcing; that is, Ocean2 is not yet at a steady state after 20 years (see Sect. 4.3), or may indicate spurious model behaviour. These three models' counterparts MITgcm-BAS and NEMO-UKESM1is are much colder, but also have known inconsistencies with the experimental protocol (sections 3.3, 3.6). The coldest temperatures in all simulations range between -2.3°C to -2.0°C, lower than the coldest -1.9°C sponge forcing temperature. These cold temperatures are generated by the melt parameterisation and occur at depth where the freezing temperature is depressed below the surface freezing point.

In the open ocean, Ocean1 temperature stratification (Fig. 2) and salinity stratification (Fig. S7) have distinct column-like features that are associated with barotropic gyres, discussed in Sect. 4.2. There is a front with a horizontal gradient in temperature below the calving front, and for some models, there is an additional front at approximately $x = 720$ km, indicating the presence of one or two gyres.

Melt rate spatial distributions in year 20 of the warm Ocean1 and cold Ocean2 COM simulations also show similarities between models (Figs. 4, 5). Melt in both experiments is enhanced at depth and near the grounding line (Fig. 6), where the thermal and haline driving is larger due to the salinity stratification and freezing point dependence on pressure. This enhancement is particularly pronounced for Ocean2, which has a steep ice shelf draft near the grounding line (Fig. 1c). Comparing Ocean1 models, the spatial distribution of melt varies, with MOM6-LAYER, MPAS-Ocean and NEMO-UKESM1is having enhanced

https://doi.org/10.5194/egusphere-2025-1942
Preprint. Discussion started: 24 June 2025

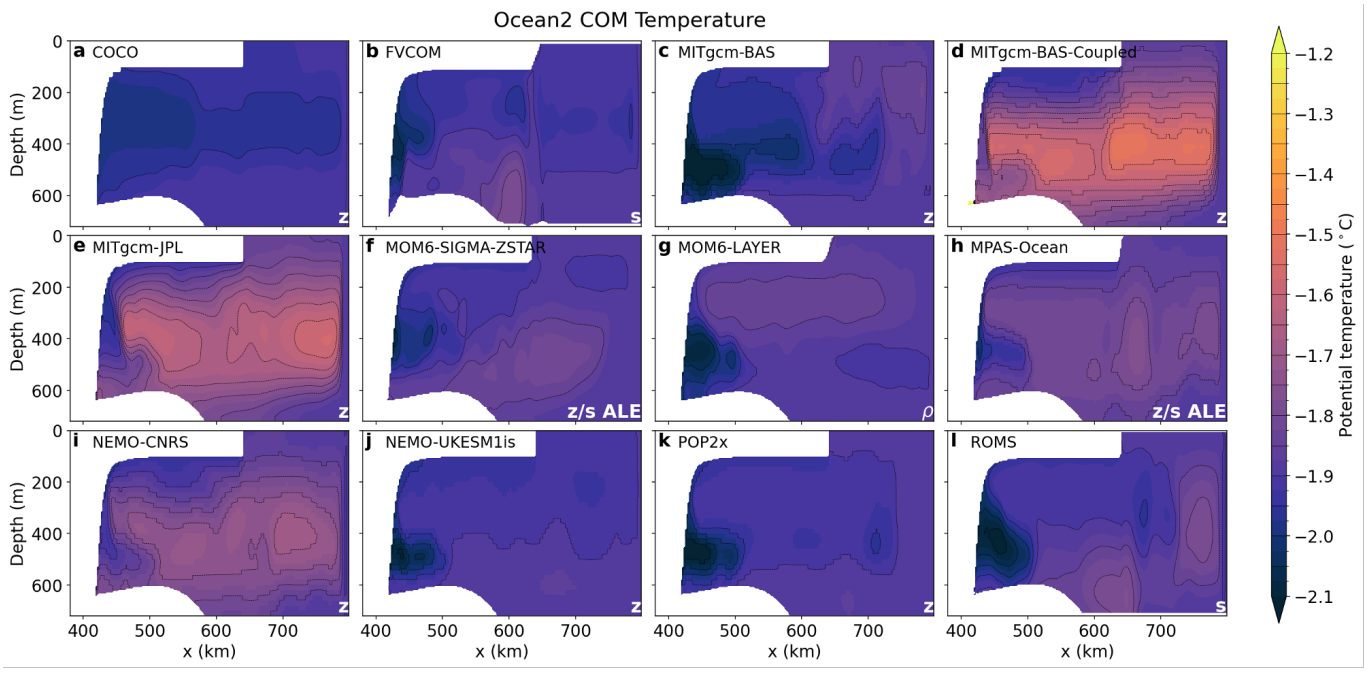

Figure 3. Steady state (average of year 20) temperature transect along $y = 40$ km in the Ocean2 COM experiment. Model vertical coordinates are labelled in the lower right corner, as in Fig. 2.

melt at the deepest grounding line (Fig. 6a). In contrast, COCO, MITgcm-BAS-Coupled and MOM6-SIGMA-ZSTAR have enhanced melt at the cavity sidewalls (Fig. 4). FVCOM has a region of freezing on the $+y$ side wall. Additionally, POP2x has a pronounced checker-board melt pattern. This striped pattern is also visible to a lesser extent in the other z-level coordinate models COCO, MITgcm and NEMO. For Ocean2, melt rates away from the deepest grounding line are small but COCO and FVCOM simulate significant freezing at the side walls (Fig. 5). COCO and FVCOM also have larger melting at depth near the grounding line (Fig. 6b) and also have cold temperatures near the ice base of the $y = 40$ km transect (Fig. 3). Other models (e.g. MITgcm-BAS, MOM6-LAYER, NEMO-UKESM1is, POP2x, ROMS) also have cold temperature transects and no such freezing, however, the temperature transects do not sample the sidewall region where freezing occurs. These variations demonstrate that models can achieve similar cavity-averaged melt rates (the tuning target melt rate below 300 m is achieved by all models except ROMS and FVCOM) with very different spatial distributions of melting. These differences in melt rate patterns, particularly near the grounding line and side walls, have implications for ice sheet evolution in coupled ice sheet–ocean models.

https://doi.org/10.5194/egusphere-2025-1942
Preprint. Discussion started: 24 June 2025

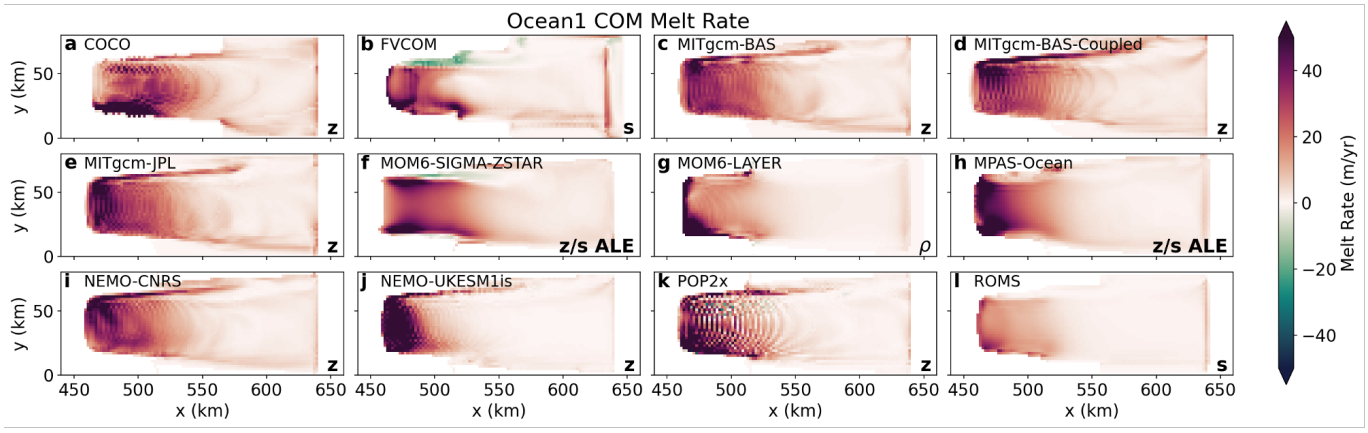

Figure 4. Steady state (average of year 20) melt rate spatial distributions for each of the 12 models in the Ocean1 COM experiment, corresponding to a warm cavity state. Model vertical coordinates are labelled, as in Fig. 2.

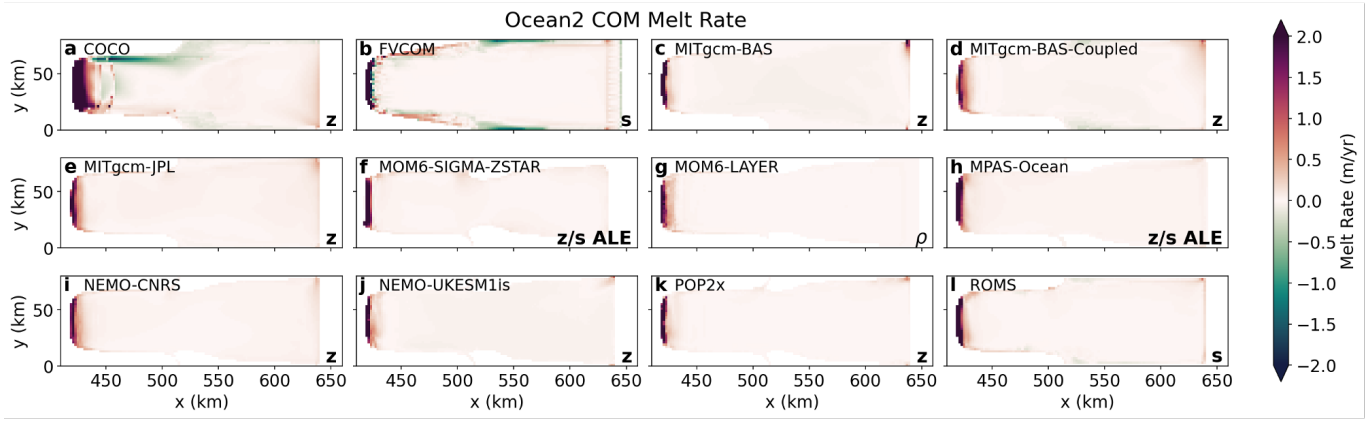

Figure 5. Steady state (average of year 20) melt rate spatial distributions for each of the 12 models in the Ocean2 COM experiment, corresponding to a cold cavity state. Model vertical coordinates are labelled, as in Fig. 2.

4.2 Steady state circulation

We present the overturning and barotropic streamfunctions for the Ocean1 and then Ocean2 COM experiments at approximately steady state (year 20). Further calculation details are in Asay-Davis et al. (2016).

The overturning circulations in year 20 of the warm Ocean1 experiments show common features across the models (Fig. 7), with upwelling occurring in the ice shelf cavity and downwelling near the northern boundary. The strength of the overturning varies between models, with most models showing maximum streamfunction values of 0.20–0.25 Sv. COCO demonstrates the strongest overturning streamfunction, with a peak value of 0.39 Sv, whilst ROMS and FVCOM have weaker circulation which is likely attributed to lower melt rates (Fig. 4, see also Fig. 11). The structure of the overturning streamfunction also varies,

https://doi.org/10.5194/egusphere-2025-1942
Preprint. Discussion started: 24 June 2025

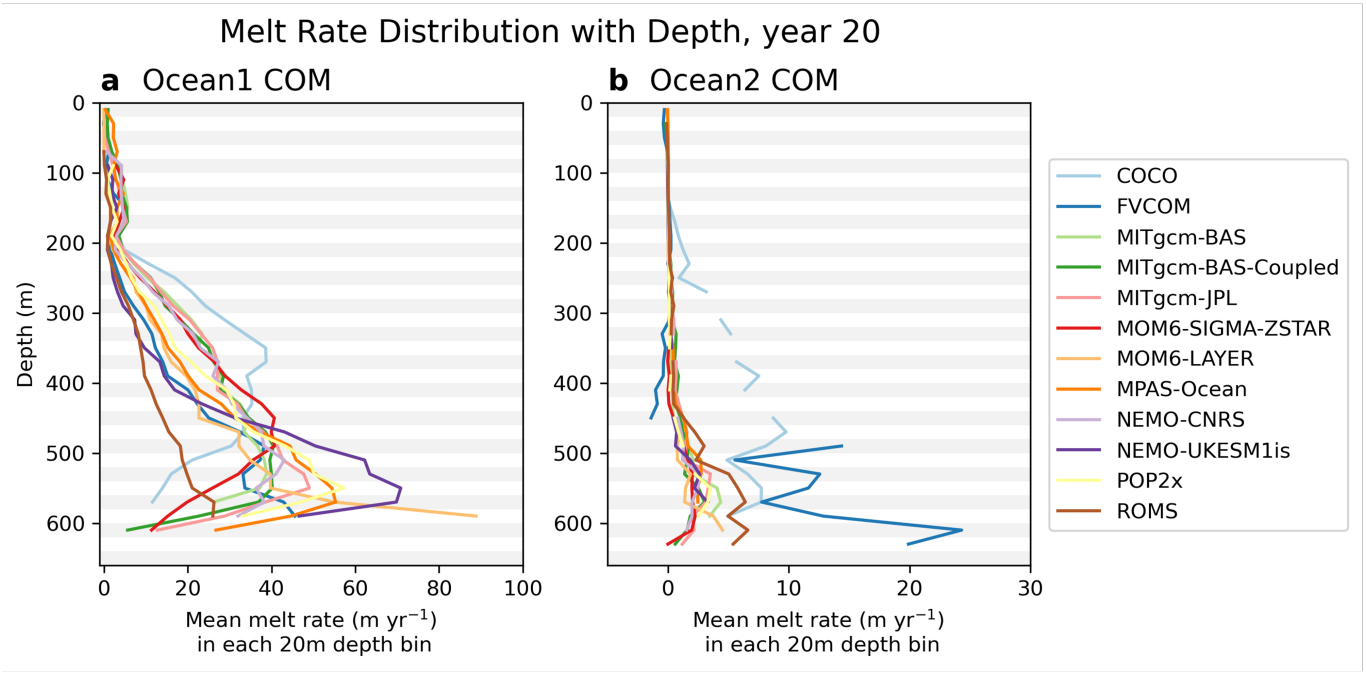

Figure 6. Melt rates averaged over year 20 as a function of ice depth, for a) the Ocean1 COM (warm) and b) the Ocean2 COM (cold) experiments. The two experiments have different geometries, Ocean2 having a steeper ice base slope over a narrower x-axis extent than Ocean1. Due to the discontinuous vertical axis and differences in ice draft between models, we plot the average melt rate in 20 m sized depth bins, indicated by the grey and white bars. Discontinuities occur when no regions of the model's ice draft are within a 20 m bin.

with some models displaying two distinct peaks, one within the ice shelf cavity and another near the "northern" (x =800 km) boundary (e.g., MITgcm-BAS-Coupled, MITgcm-JPL, NEMO-CNRS), and others exhibit a single peak near the northern boundary (e.g., FVCOM, MITgcm-BAS, MPAS-Ocean, POP2x, ROMS).

The barotropic streamfunctions in year 20 of the warm Ocean1 experiments reveal similar circulation patterns across most models within the ice shelf cavity, with the exception of COCO (Fig. 8 in the ice shelf cavity and see Fig. S5 for the full domain). The typical pattern involves a "western"-intensified ($y > 50$ km) clockwise circulation within the cavity, with a maximum barotropic streamfunction of 0.26 ± 0.17 Sv in this region ($y > 50$ km, $x < 640$ km). The circulation feature varies in shape, with some models having strongly boundary-intensified circulation (e.g. MITgcm-BAS) while others are centred further away from the boundary (e.g. MOM6-SIGMA-ZSTAR), and the extent that the circulation penetrates towards the grounding line also differs between models. However, COCO deviates from this pattern, with only a weak western boundary flow and instead a strong counterclockwise circulation within the ice shelf cavity. This circulation is potentially linked to a spatial pattern of ice shelf melt with peaks along the "eastern" ($y < 30$ km) boundary of the ice shelf cavity, in contrast to many other models (Fig. 8). In this eastern region of the ice shelf cavity, there are differences in circulation between all models (e.g. differences in location of the grey, solid 0 Sv line in Fig. 8), and in particular, the MOM6 models display a large counterclockwise circulation. Variation

https://doi.org/10.5194/egusphere-2025-1942
Preprint. Discussion started: 24 June 2025

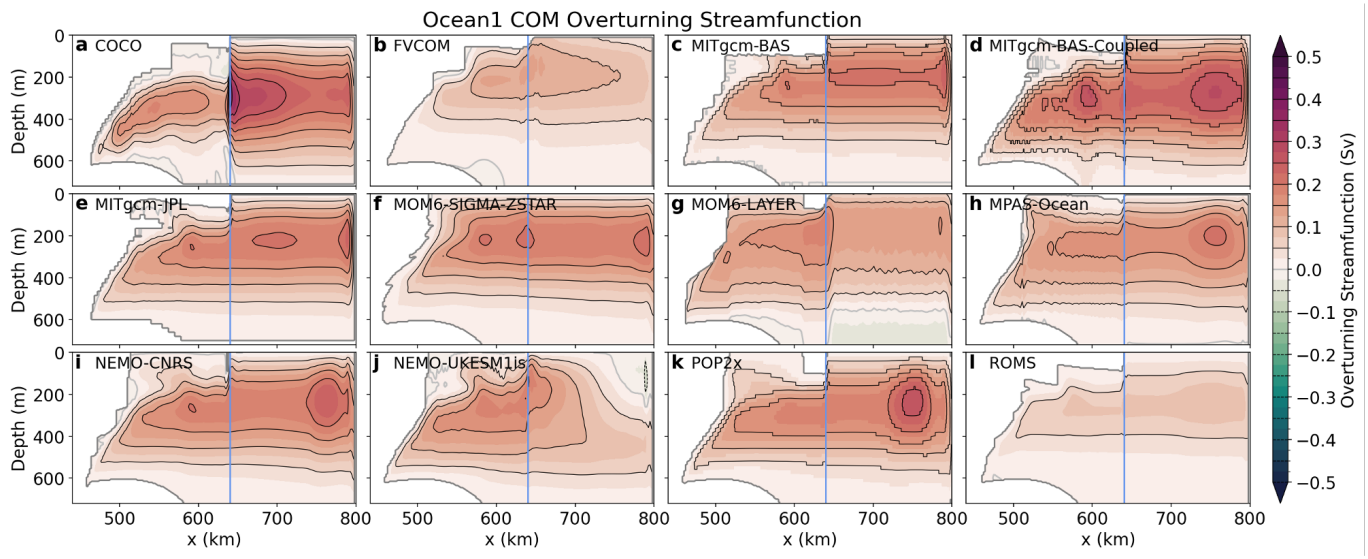

Figure 7. Ocean1 COM zonal mean overturning streamfunctions in depth coordinates averaged over year 20, corresponding to the steady warm state of the cavity. The 0 Sv contour is indicated by a light grey line and the ice front at $x = 640$ km is indicated by a blue line.

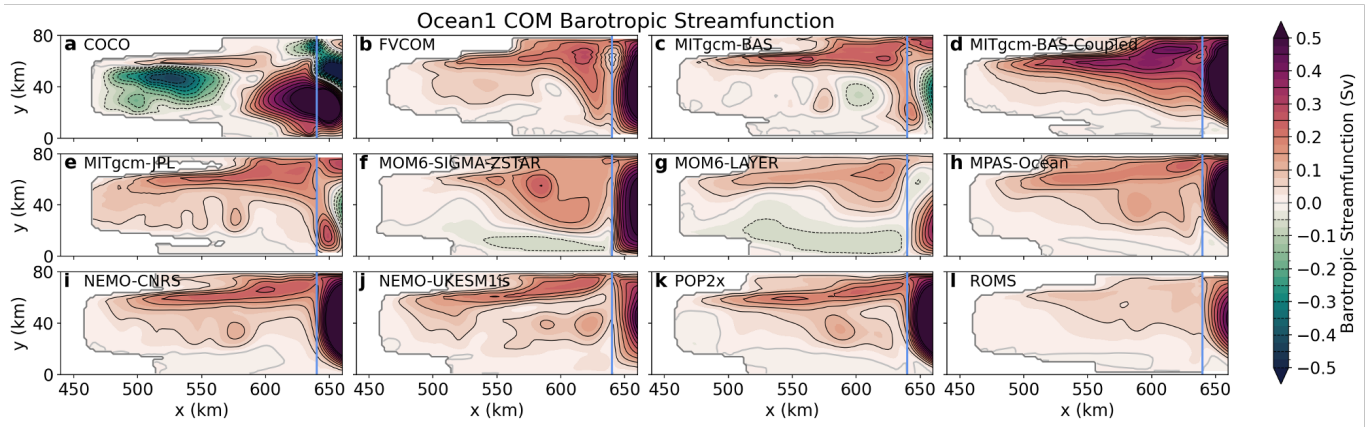

Figure 8. Ocean1 COM barotropic streamfunction averaged over year 20, corresponding to the steady warm state of the cavity. We restrict the range of the x-axis to the ice shelf cavity; an extended version is shown in Fig. S5. The 0 Sv contour is indicated by a light grey line and the ice front at $x = 640$ km is indicated by a blue line.

in circulation between models may be associated with the different interpolation and smoothing choices of the topography and ice draft (Sect. 3, Figs. S11, S12) and are likely also related to the different melt rate spatial distributions (Figs. 4, 5, 6).

Moving further towards the open ocean, the warm Ocean1 barotropic streamfunctions show a clockwise inflow and outflow of water crossing beneath the ice shelf calving front at x =640 km. This flow, quantified by the maximum barotropic stream-
435 function near the ice front (630 km< x <650 km), varies in magnitude (0.41 ± 0.27 Sv), with models with higher barotropic

https://doi.org/10.5194/egusphere-2025-1942
Preprint. Discussion started: 24 June 2025

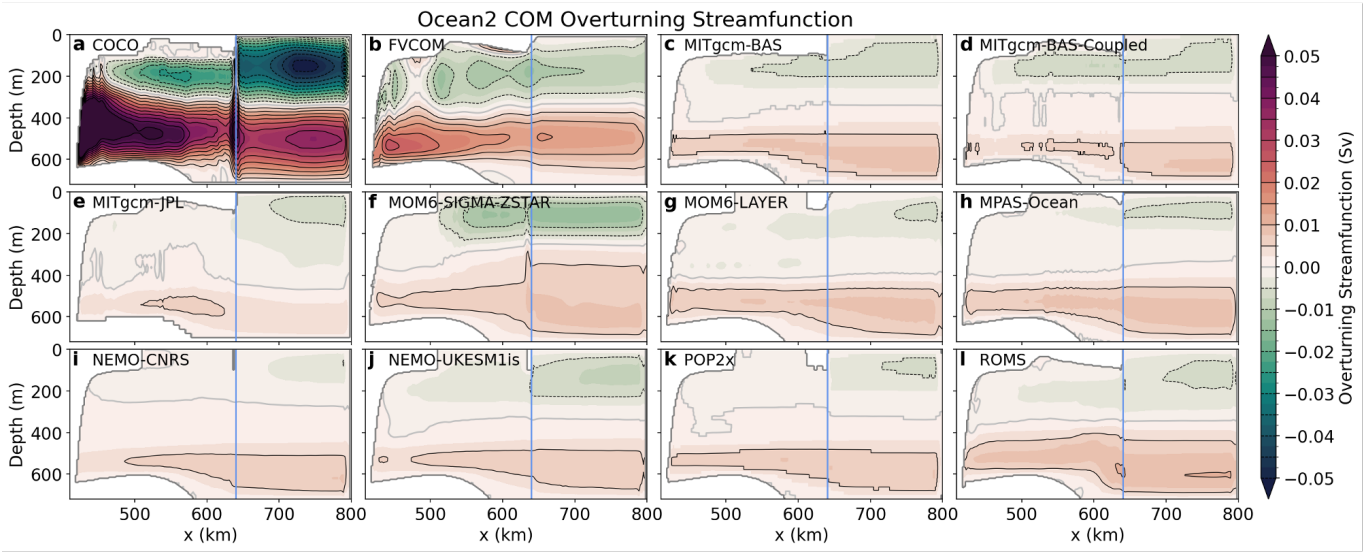

Figure 9. Ocean2 COM zonal mean overturning streamfunctions in depth coordinates averaged over year 20, corresponding to the steady cold state of the cavity. The 0 Sv contour is indicated by a light grey line and the ice front at $x = 640$ km is indicated by a blue line.

streamfunctions also typically having higher overturning streamfunctions. Despite the general similarity in ocean circulation within the ice shelf cavity, the ocean circulation outside the ice shelf cavity shows significant variability among the models (Fig. S5). Some models have two open ocean gyres, with no consistent rotation direction between models, whilst other models (e.g. FVCOM, MOM6-SIGMA-ZSTAR) have just one gyre (and the number of gyres can vary with time). These open ocean gyres are sensitive to the discretisation of the ice shelf geometry in the MISOMIP1 configuration (Zhao et al., 2022) and may also be sensitive to the model implementation of the northern boundary restoring region.

In the cold and steep ice base Ocean2 experiments at year 20, the overturning circulation consists of an opposing two-cell structure across most models, with a clockwise circulation at deeper levels and a counterclockwise circulation at shallower depths (Fig. 9). This circulation can be explained by a buoyant meltwater current that rises beneath the steep ice base near the grounding line until it reaches its neutral buoyancy and separates from the ice shelf (Holland, 2017). Return flow above and below this depth is created by the modifications made by the restoring forcing to the fluid's buoyancy at the $x = 800$ km wall boundary. The similar cell separation height across models (grey solid line in Fig. 9) suggests that the neutral buoyancy depth places a strong constraint on the vertical overturning structure. Typical circulation strengths are 8.2 ± 2.4 mSv for the deep clockwise circulation and -7.6 ± 2.4 mSv for the shallower counterclockwise circulation for all models except COCO and FVCOM. COCO and FVCOM show overturning strengths about 14 and 3 times larger than the other models, respectively. The separation of the meltwater current from the ice draft at its neutral buoyancy depth also explains the lack of freezing in the models (Fig. 5). Additionally, the flow resembles the mixed-source circulation observed inside Antarctic cold cavity ice shelves (Hattermann et al., 2021; Janout et al., 2021).

https://doi.org/10.5194/egusphere-2025-1942
Preprint. Discussion started: 24 June 2025

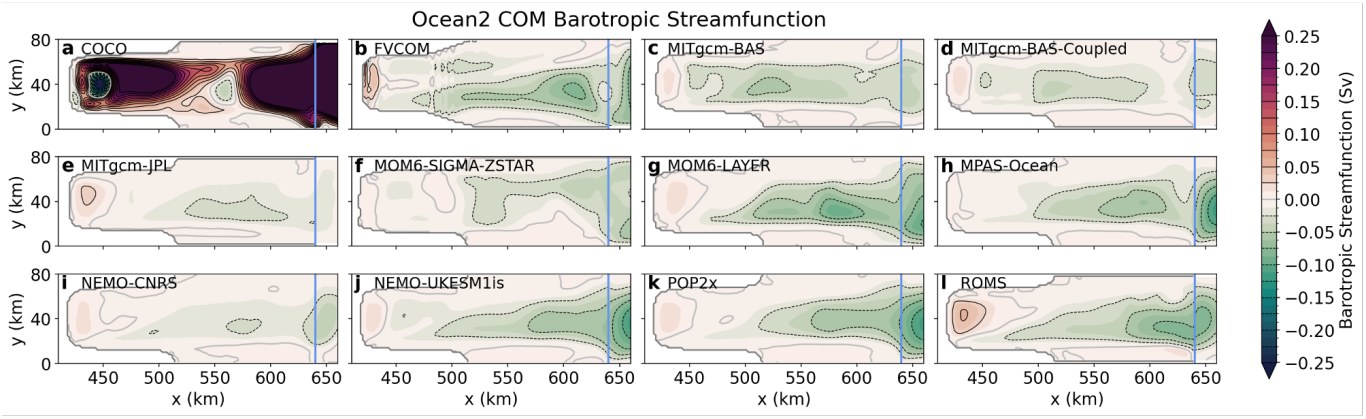

Figure 10. Ocean2 COM barotropic streamfunction averaged over year 20, corresponding to the steady cold state of the cavity. We restrict the range of the x-axis to the ice shelf cavity; an extended version is shown in Fig. S6. The 0 Sv contour is indicated by a light grey line and the ice front at $x = 640$ km is indicated by a blue line.

The barotropic streamfunction in the cavity (Fig. 10; see Fig. S6 for the full domain) at year 20 of the cold Ocean2 experiments generally shows a similar circulation pattern across models, except for COCO. Most models exhibit weak clockwise circulation near the grounding line (maximum streamfunction for $x < 460$ km is 47 ± 42 mSv) and counterclockwise circulation in the outer ice shelf cavity (minimum negative streamfunction inside the cavity for $x > 460$ km is -75 $\pm$ 43 mSv), though circulation patterns differ. In contrast, circulation in COCO once again differs significantly from other models, consisting of two strong clockwise circulations within the ice shelf cavity. These circulations have peaks in both the inner and outer cavity, showing circulation strengths of 0.29 Sv and 1.2 Sv, respectively. Despite the similarities in simulated ocean circulation within the ice shelf cavities, the circulation patterns outside the ice shelf cavity differ significantly (Fig. S6), consistent with the findings from the Ocean1 experiment.

The circulation results for both the Ocean1 and Ocean2 experiments suggest that (a) most ISOMIP+ ocean models are capable of simulating similar ocean circulation structures within the ice shelf cavity, which are only weakly influenced by the off-shelf ocean circulation, underscoring the robustness of these models, and (b) differences in the treatment of ocean boundaries and sponge layers among the models and model geometries may contribute to the observed discrepancies.

4.3 Transient melting

In this section, we explore the transient nature of the ISOMIP+ Ocean1 and Ocean2 COM ice shelf cavity experiments where the ocean's initial conditions adjust to the forcing at the northern boundary. The melt rate changes as temperature and salinity changes are advected into the cavity, and there are feedback mechanisms between melting and the barotropic and overturning circulation.

The area-averaged melt rates over the entire ice shelf for the Ocean1 and Ocean2 experiments demonstrate the dependence of melt rate on temperature (Fig. 11). The Ocean1 melt rate increases from its low baseline created by the cold initial conditions

https://doi.org/10.5194/egusphere-2025-1942
Preprint. Discussion started: 24 June 2025

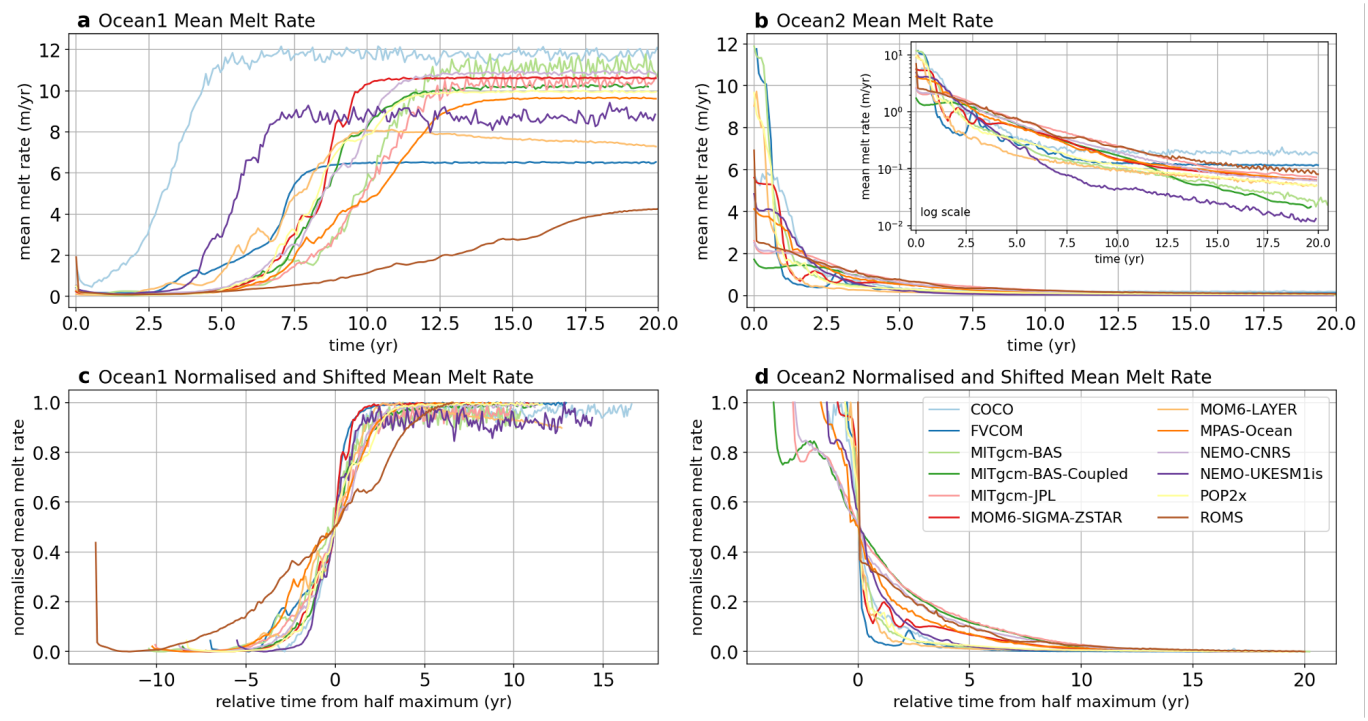

Figure 11. Area-averaged melt rate over the entire ice shelf for the (a) Ocean1 COM and (b) Ocean2 COM experiments, showing a spin-up and spin-down respectively of the overturning circulation over time. Panels (c) and (d) normalise the melt rate by the maximum melt rate and shift the time axis such that their midpoints are at time zero for each experiment.

as the warm boundary forcing penetrates the cavity. Melt rates approach a constant value for all models by year 14, except for ROMS which is still increasing in year 20 (Fig. 11a). The quasi-steady mean melt rates vary significantly across models (4-12 m yr^{-1}) and some models (COCO, MITgcm-BAS, NEMO-UKESM1is and MPAS-Ocean) show larger temporal variability in melt rate with $\sim$1 m yr^{-1} variation in the monthly averaged data. These maximum area-averaged melt rates are lower than the target 30 m yr^{-1} of the Ocean0 tuning experiment, which matches the steady state Ocean1 conditions, because the Ocean0 tuning only considers the ice shelf cavity regions deeper than 300 m (recall that all models except FVCOM and ROMS achieved the Ocean0 target melt rate). The large variation in the final ice shelf cavity-averaged melt rate highlights the importance of the spatial distribution of melt (Fig. 4a), particularly as a function of depth (Fig. 6). Additionally, the time taken for the model spin-up to reach a steady state varies between the models, with COCO reaching steady melt rates within 5 years but ROMS still increasing in melt at year 20. However, after an initial spin-up phase, most models show a similar transition time during which the melt rates increase in response to the warming cavity, as demonstrated in Fig. 11c. Here, the melt rates are normalised by their maximum value and shifted by the earliest time they achieve a melt rate of half their maximum melt rate. The models merge into one sigmoid-like profile with an approximate width of 5 years, except for ROMS. This similarity indicates that

https://doi.org/10.5194/egusphere-2025-1942
Preprint. Discussion started: 24 June 2025

differences in spin-up time are more likely to be associated with the timescales for which the boundary forcing propagates into the ice shelf cavity rather than different circulation responses to changing melt rates.

The Ocean2 melt rates decrease from relatively high values, due to the warm initial conditions, towards melt rates of less than $2\,\mathrm{m\,yr^{-1}}$ within 2 years, in response to the advection of the colder water from the restoring into the cavity (Fig. 11b). The logarithmic scale inset demonstrates that the resultant melt rates at 20 years still vary by an order of magnitude between 0.01–0.2 $\mathrm{m\,yr^{-1}}$, and additionally that many of the models have not yet reached steady state, a possible explanation for the remnant warm temperatures in some of the year 20 temperature transects (Fig. 3). When scaled and shifted in time (Fig. 11d), the models are similarly described by a sigmoid-like profile, though there are some exceptions with a rebound in melt rate in MITgcm-BAS-Coupled and MITgcm-JPL after $\sim$2 years, possibly related to the development of a melt-circulation feedback or a result of the advection scheme producing spuriously warm water (Sect. 3.3).

The different initial (slower) spin-up and (faster) spin-down timescales in the Ocean1 and Ocean2 experiments, respectively (Fig. 11), can be explained by the timescales of advection of temperature anomalies by the overturning circulation, as well as the differing ice geometries in the two experiments. Since the boundary conditions and initial conditions have the same density stratification (Fig. 6 of Asay-Davis et al., 2016), the only source of density variations is ice shelf melting (Holland, 2017), which is guided by the temperature of the cavity. In the Ocean1 simulation, warm water is slowly advected from the boundary to the base of the initially cold Ocean1 ice shelf by the weak cold cavity state circulation, leading to low melt rates for $\sim$5 years for most models. Once warm intrusions arrive at the ice shelf base, they drive increased melt and buoyancy-driven overturning, which advects warm boundary water into the cavity more quickly in a feedback mechanism that further spins up the circulation. The colder-restoring Ocean2 begins with a fast warm cavity state circulation, rapidly slowed by the cold temperature intrusion as the melting drops, to become a weak circulation. The flow also separates from the ice at mid-depth (Fig. 9), further reducing melt and circulation. The slower circulation in Ocean2 therefore increases the time required to "flush" the cavity with the boundary conditions and equilibrate, explaining why most models have reached a steady state by the end of Ocean1, but not Ocean2. Additionally, the difference in ice base geometries between Ocean1 and Ocean2 (Fig. 1) likely contributes to this asymmetric behaviour. However, similar asymmetries in warming and cooling transient melt rate responses are seen in fixed geometry simulations with an oscillating far-field forcing, such as in the Ocean1 domain (Zhou et al., 2024) and in wedge-like ice shelf setups (Holland, 2017).

We also compare the relationship between ocean temperatures and melting. For the Ocean2 experiments, melt rates scale approximately quadratically with ocean temperatures near the front of the cavity (or more specifically, the thermal forcing at the front of the cavity, taken as the difference between the ocean temperature and a reference freezing point at depth of -2.1°C, has a log-log best-fit power-law exponent with melt of $n \approx 2$ on average in Fig. S1b). This relationship is consistent with the quadratic equilibrium response of the melt rate to thermal forcing shown in Holland et al. (2008) and Holland (2017). The Ocean1 simulations have a different scaling (close to linear with $n \approx 1.3$, see Fig. S1a) associated with the cavity being in a transient state. This transient state can be explained by the observed delay in spin-up due to weak circulation despite warming ocean temperatures near the front of the cavity. The deviation from the quadratic scaling is consistent with Holland (2017),

https://doi.org/10.5194/egusphere-2025-1942
Preprint. Discussion started: 24 June 2025

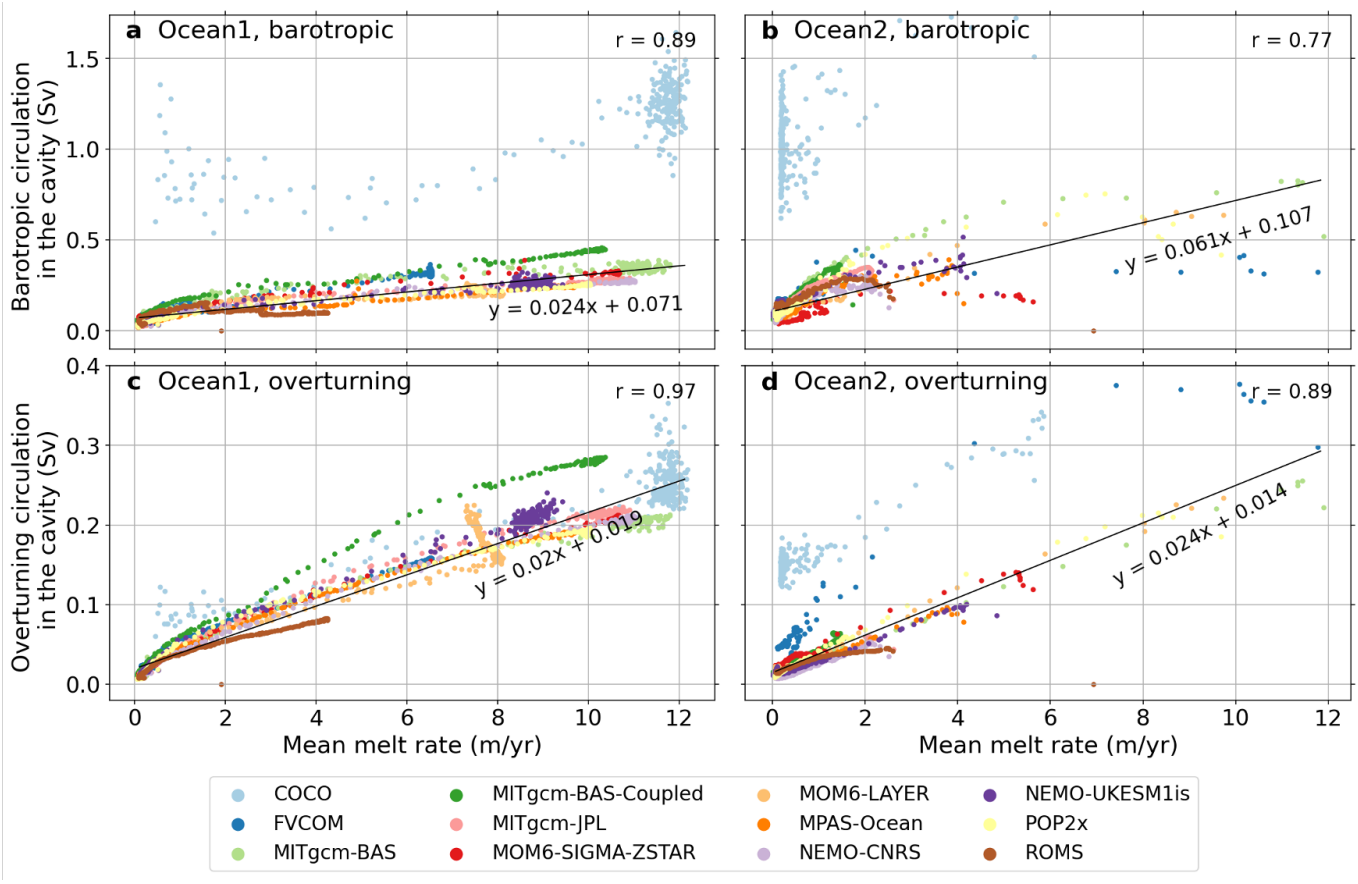

Figure 12. Strength of the barotropic (upper) and overturning (lower) streamfunctions as a function of area-averaged melt rate for the Ocean1 COM experiments (left) and Ocean2 COM experiments (right). Circulation strength is determined from the maximum minus minimum streamfunction values in the cavity, i.e. for x <640 km. Each scatter point represents a different month of data. Linear lines of best fit and Pearson correlation coefficients include all data except for the COCO model.

who show that warm-to-cold transitions (i.e. Ocean2) better match the equilibrium response compared with cold-to-warm transitions (i.e. Ocean1).

The ISOMIP+ experiments demonstrate a strong relationship between melt rate and circulation across models and forcings. Fig. 12 shows the barotropic and overturning circulation strength, calculated from the difference between maximum and minimum streamfunction amplitudes within the ice shelf cavity, as a function of area-averaged melt rate for each month of the Ocean1 and Ocean2 simulations. Most models follow shared linear relationships between melt rate and overturning and barotropic streamfunctions for both the Ocean1 and Ocean2 experiments. Additionally, the multi-model mean gradients of the overturning and barotropic streamfunction as a function of melt have the same order of magnitude, indicating barotropic and overturning circulation have similar magnitudes. Consistent with previous circulation metrics (Fig. 8 and 10), the COCO

https://doi.org/10.5194/egusphere-2025-1942
Preprint. Discussion started: 24 June 2025

barotropic streamfunction is abnormally strong in both experiments, suggesting the influence of a circulation source other than melting. Deviation from the linear relationship between melt and circulation strength may be explained by the circulation being influenced by the restoring at the boundary in addition to the expected buoyancy forcing from melting. If the ice shelf cavity flow is driven only by buoyancy, the magnitude of melt would be expected to be proportional to the near-ice velocity, which in turn should approximately scale with overturning circulation strength (e.g. MacAyeal, 1984; Jourdain et al., 2017). In this buoyancy-driven flow regime, the barotropic ice shelf cavity flow is mostly geostrophic and driven by the density difference between the buoyant meltwater and deep ocean restoring water properties, therefore, barotropic flow would also scale linearly with melt (e.g. Jenkins, 2016; Jourdain et al., 2017; Finucane and Stewart, 2024). However, note that geostrophy does not hold near boundaries due to the presence of boundary drag, but the boundaries of the ice shelf cavity contain regions with significant melt (e.g. $y > 60$ km in Fig. 4). Understanding the ocean dynamics involved in the coupled melt rate–circulation relationship requires further experiments not performed here.

Despite both Ocean1 and Ocean2 having linear circulation–melt relationships, correlations are weaker in Ocean2 (Fig. 12b,d). The overturning metric in Ocean2 quantifies the speed of the mid-depth flow away from the ice shelf as the meltwater flow separates from the ice (Fig. 9), and is therefore less tightly coupled to the melt rate averaged across the whole ice shelf than in Ocean1. Additionally, the reduction in the strength of the correlation between melt and circulation in Ocean2 may be due to weaker circulation strength, which would increase the importance of boundary layer temperature and salinity properties that change with melting. The prescribed tidal friction velocity (acting to increase the melt compared to that expected by the boundary layer velocity) may contribute to the non-zero intercepts of the circulation–melt relationships, which is more prominent in the slower Ocean2 experiments (Fig. 12).

Despite the deviations in some models from the linear circulation–melt relationship, Fig. 12 demonstrates agreement in the circulation–melt relationship amongst the models. This model agreement is promising, showing reliability in simulated ocean-ice interactions and feedback processes between circulation and melt. The circulation–melt relationship is thus an important metric for model comparison, where models display agreement despite individual melt rate or temperature distributions.

4.4 Differences and drivers of melt rate

Differences in melt rate between models can be understood by considering the driving factors of ice shelf basal melt. Much of these differences can be attributed to (a) the differences in the representation of the temperature and salinity properties in the boundary layer region, and (b) model choices of calculating the thermal and haline driving and the distribution of heat and meltwater fluxes.

The representation of the ice shelf–ocean boundary layer in the Ocean1 COM models at year 20 is shown in Fig. 13, when the cavity is in a warm state. Here, we show the potential temperature in the upper ice shelf cavity, where the vertical coordinate is the distance from the ice shelf basal surface. This remapping produces the jagged features of Fig. 13: model output is remapped onto a discrete grid with 5 m vertical spacing, whereas the ice draft can vary continuously. Therefore, the distance from the ice (the difference in depth, i.e. the difference between ice draft crosses and 5 m output in Fig. S13) has both discrete and

https://doi.org/10.5194/egusphere-2025-1942
Preprint. Discussion started: 24 June 2025

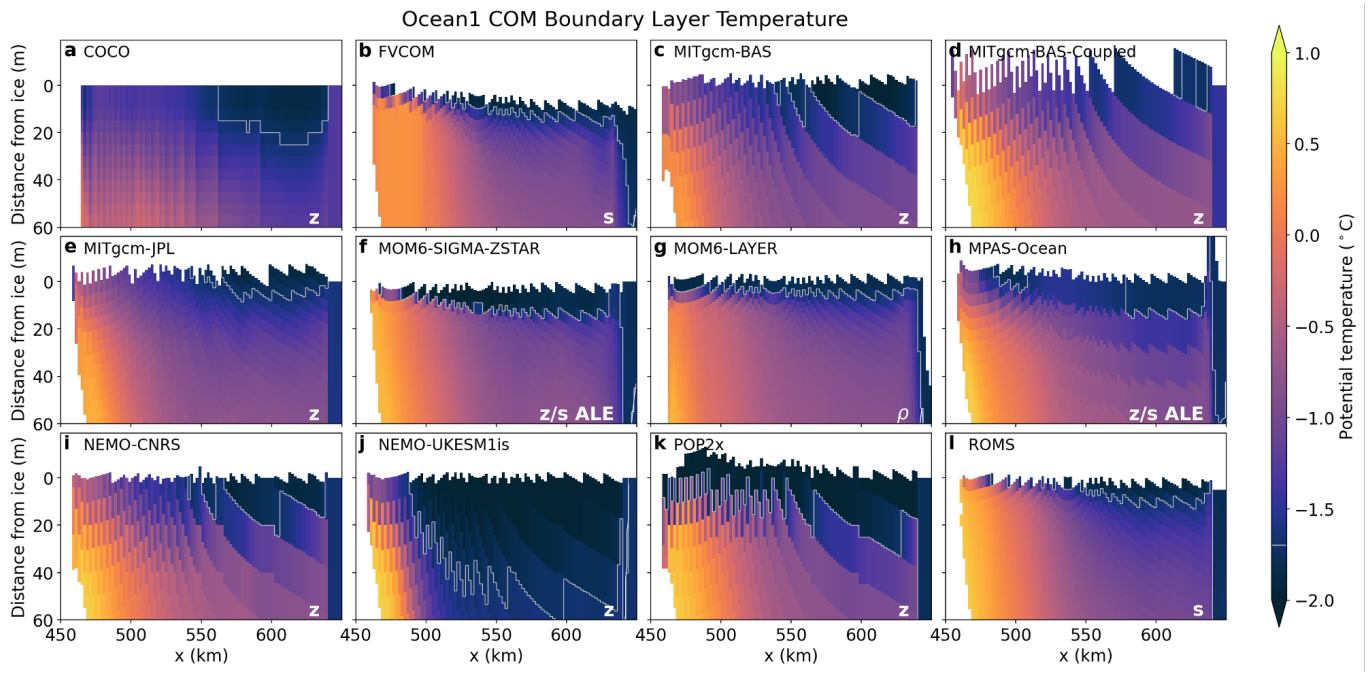

Figure 13. Boundary layer temperature transect averaged over year 20 of the Ocean1 COM experiment. The temperature transect of Fig. 2 is remapped in the vertical direction to be the distance away from the ice (taken from the difference between the remapped model output on a 5 m resolution grid to the ice draft, which can be values not on the 5 m grid, leading to jagged shapes; see Fig. S13). Model vertical coordinates are labelled, as in Fig. 2. The -1.7°C contour is shown in white.

continuous components and is jagged in shape. Additionally, the distance can be negative if the depth to which the ocean model output is remapped is shallower than the ice draft (e.g. MITgcm-BAS-Coupled, Fig. S13d).

Comparing boundary layer temperature profiles, most Ocean1 models show warmer water at depth away from the ice base (Fig. 13). Conditions are particularly warm (greater than 0.5 °C) near the ice base in the deeper portions of the cavity (e.g. x-coordinate of 450-500 km), but models show different widths in the x-direction of this warmer water band. Upslope of this warm region ($x > 500$ km), there is a transition to cooler temperatures (∼-1.1 – -0.025°C). Above this, and directly below the ice shelf, there is a cold layer (the ice shelf meltwater; approximately <-1.7°C, shown in white contours in Fig. 13). All the Ocean1 COM models simulate these features but with different horizontal and vertical scales. Ice shelf–ocean boundary layers in the cold Ocean2 COM models are colder and thicker than Ocean1, but also exhibit inter-model variation (Fig. S2) and may be associated with the models not yet reaching equilibrium (Fig. 3, 11).

Focusing on the meltwater layer closest to the ice shelf–ocean boundary, Ocean1 COM models have different temperature profiles (Fig. 13; see Fig. S2 for Ocean2 COM results). Some models have a thin, cold layer that transitions smoothly and relatively rapidly into warmer water below, e.g. FVCOM, MITgcm-JPL, MOM6-SIGMA-ZSTAR, MOM6-LAYER and ROMS: mostly the terrain-following and isopycnal coordinate models (note the 5 m resolution output may also hide part of

https://doi.org/10.5194/egusphere-2025-1942
Preprint. Discussion started: 24 June 2025

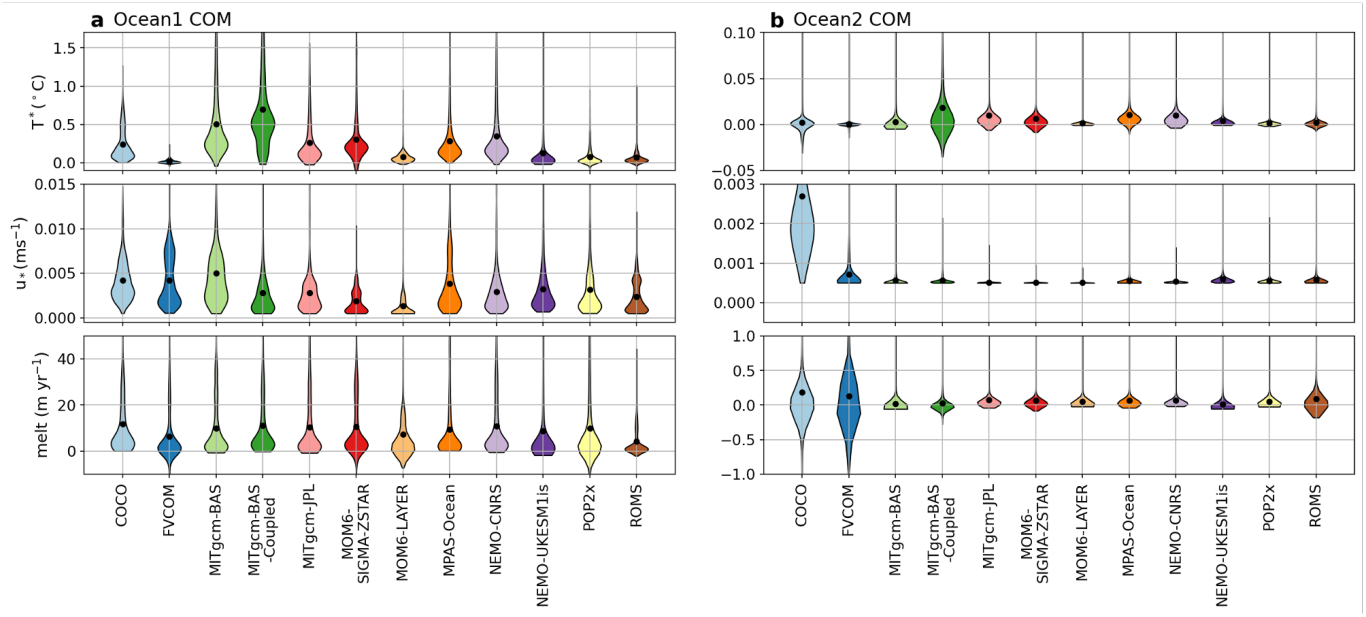

Figure 14. Statistical distributions in space of thermal driving (T^*), friction velocity (u_*) and melt for each model and Ocean1 and Ocean2 COM experiments, averaged over year 20. Black dots represent the spatial mean values.

the thin, cold boundary layers in ROMS and FVCOM, e.g. ROMS has top layer thicknesses less than 5 m). Some models have a cold layer but with a thicker extent (MITgcm-BAS, MITgcm-BAS-Coupled, MPAS-Ocean, NEMO-CNRS and NEMO-UKESM1is). Sharp differences in temperature along the meltwater layer suggest that the z-coordinate resolution is partially responsible. Lastly, some other models have a largely unique representation of the boundary layer, being much thicker than the other models (COCO and NEMO-UKESM1is, the latter of which has known erroneous surface cooling). POP2x also has a very cold boundary layer, likely related to its large melt rate transfer coefficient (Table 2) compared to other z-coordinate models. Boundary layer representations are therefore dependent on the vertical coordinate, with terrain-following coordinates tending to have thinner boundary layers, likely due to their higher vertical resolution beneath the ice shelf and reduced implicit mixing (in models that distribute meltwater over only the uppermost layer). However, other model-specific numerics may also play a role, noting significant differences in boundary layer representation even between z-coordinate models with the same vertical resolution. These differences may be associated with different implementations of the Losch (2008)-style sampling and meltwater distribution layer, as well as partial cell thicknesses. The simplified, prescribed diffusivities of the ISOMIP+ COM protocol may also be an important controller of boundary layer representation compared to model mixing parameterisations used in typical realistic model configurations (equivalent results for TYP configurations shown in Fig. S9, S10). In summary, Fig. 13 demonstrates that the ice–ocean boundary temperature profile is a key metric of variability between models.

Ice shelf–ocean boundary layer temperature is one controller of melting that differs between models. However, the strength of the friction velocity is also included in the basal melt parameterisation, as are the transfer coefficients. Fig. 14 shows the

https://doi.org/10.5194/egusphere-2025-1942
Preprint. Discussion started: 24 June 2025

distribution of thermal driving (defined as the difference between the far-field and boundary layer temperature in the melt parameterisation; $T_w - T_{z_d}$ in Eqn. 3), friction velocity and melt over the cavity averaged over year 20, noting that the product of thermal driving and friction velocity is scaled by the transfer coefficients (which differ between models) and other constants to determine melt. Thermal driving in Ocean1 is generally larger in the models with thicker boundary layers, mostly z-level models that use a 20 m layer to sample temperature and salinity that may extend deeper into the warm cavity interior than the meltwater layer (e.g. COCO, MITgcm-BAS, MITgcm-BAS-Coupled, MITgcm-JPL and NEMO-CNRS). z-level models also tend to have slightly larger friction velocities, possibly also associated with a deeper sampling depth. The spatial distribution of melt rates with depth (Fig. 6) is associated with both thermal driving and friction velocity distributions, where model variation in the location of peak melt rate is associated with the friction velocity (and therefore circulation) as well as increasing thermal driving with depth. In Ocean2, there are large differences in the distribution of thermal driving, whereas friction velocities are small and for all but COCO (which has an anomalously strong barotropic circulation, Sect. 4.2) display a nearly spatially uniform friction velocity of $5 \times 10^{-4}\,\mathrm{m\,s^{-1}}$, which is the minimum prescribed tidal velocity scaled by the drag coefficient. Fig. 14b also highlights the significant portions of the COCO, FVCOM, ROMS and MITgcm-BAS-Coupled cavities that are freezing at the ice shelf-ocean interface rather than melting.

One of the key parameters in the experiment is the heat and salt transfer coefficients of the three-equation parameterisation, which control the melt rate and, therefore, circulation. To verify the implementation of the basal melt parameterisation, diagnosed melt rates (and hence applied meltwater fluxes) are compared with the product of the diagnosed thermal driving and friction velocity in the Ocean1 and Ocean2 COM models (Fig. S3). The melt rate is scaled by constants in Eqn. 3, including model-dependent transfer coefficients (Table 2). POP2x shows some deviations from the diagonal 1:1 line, possibly indicating transient numerical inaccuracies. The MITgcm-BAS-Coupled simulation has a slope of 1 only if a readjusted transfer coefficient is used rather than the value initially reported (see Sect. 3.3 for more details), as does the Ocean1 simulation of MITgcm-BAS, which has a systematically different slope from the Ocean2 simulation. As discussed in Sect. 3.3, the transfer coefficients used may have differed from the reported values, or there was a diagnostics error. Nevertheless, the z-level models tend to have similar transfer coefficients between 0.0135 and 0.0325 (Table 2) with some exceptions: NEMO-UKESM1is requires a larger coefficient to offset its erroneous cooling, MITgcm-BAS has inconsistent transfer coefficients, and POP2x has an anomalously large transfer coefficient that we do not have an explanation for. The other z-level model configuration transfer coefficients are generally smaller than that for the terrain-following, ALE and isopycnal coordinates (Table 2). z-level models are expected to require smaller transfer coefficients to achieve the same tuned melt rate, since the lower vertical resolution near the ice and greater thermal driving sampling and freshwater flux distribution distances result in larger melt rates compared with higher resolution terrain-following configurations (Gwyther et al., 2020).

To verify the simulated representation of ice–ocean thermodynamics in the models, we assess the water mass evolution in the warming Ocean1 experiment (Fig. 15). In the absence of other heat and freshwater sources, water mass properties should eventually be confined between the restoring conditions and the meltwater mixing line (Gade, 1979), along which a given water mass will cool and freshen at a constant ratio when interacting with the ice shelf at different depths. Neglecting heat conduction into the ice, as in the experimental protocol (Asay-Davis et al., 2016), the slope of these characteristic lines in

https://doi.org/10.5194/egusphere-2025-1942
Preprint. Discussion started: 24 June 2025

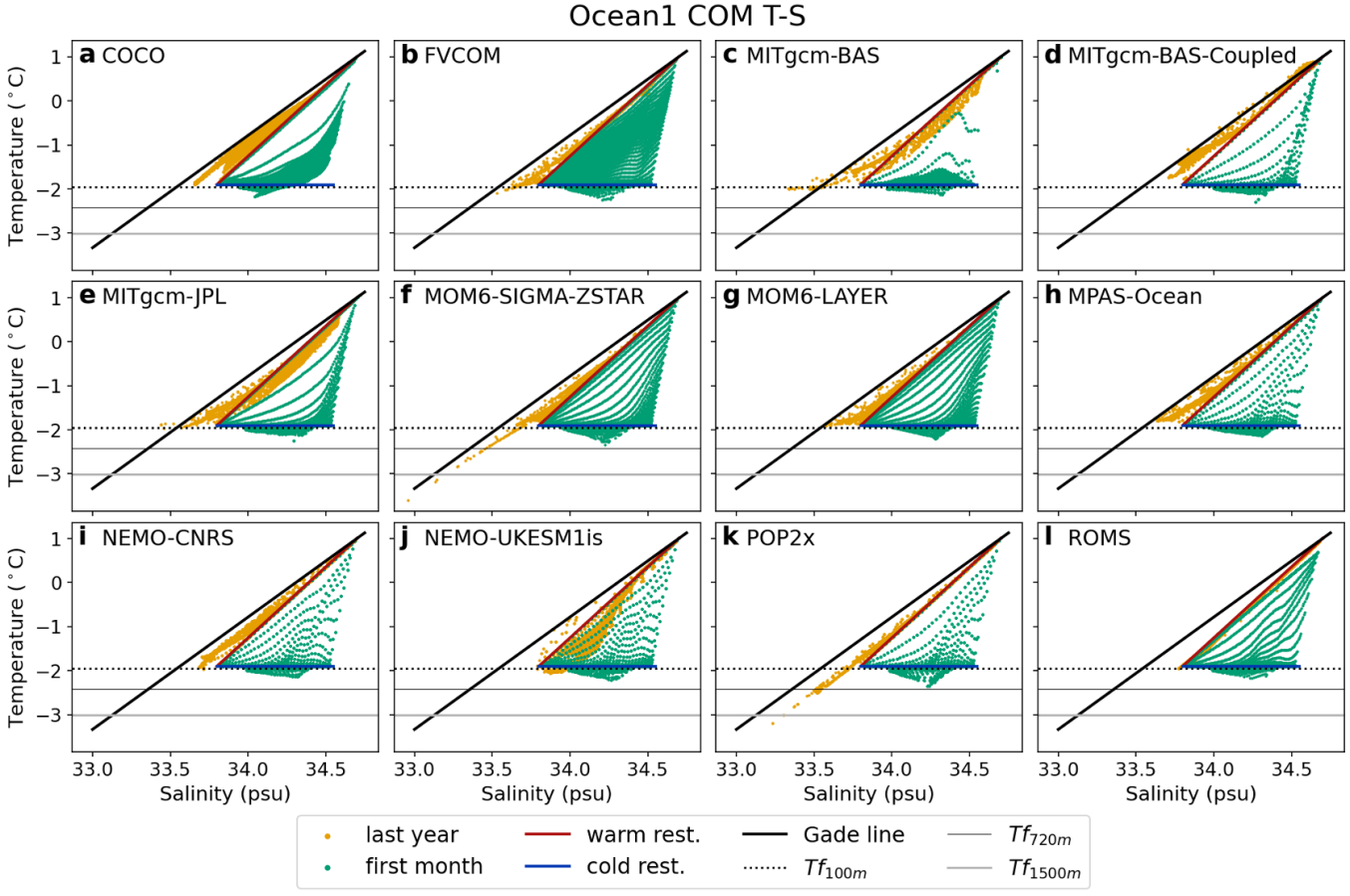

Figure 15. Temperature–salinity space verification of Ocean1 COM experiments. Model output averaged over the first month is shown in green, and averaged over the last year (year 20) in yellow. The warm and cold restoring profiles are shown by red and blue lines, respectively. The Gade line (see Eqn. 6 for definition) is shown, indicating the meltwater mixing line in temperature–salinity space. Freezing points calculated from Eqn. 2 are shown for three depths: 100 m, 720 m (the maximum domain depth) and 1500 m. Ocean2 results are in Fig. S4.

temperature–salinity (T–S) space are given by

$$\frac{\partial T}{\partial S} = \frac{T_w - T_f + L/c_w}{S_0}, \tag{6}$$

(Gade, 1979; Jenkins and Holland, 2007). Here, the specific heat capacity of seawater c_w and latent heat of fusion L are presented in Table 1. The salinity S_0 of the seawater in contact with the ice is taken as a constant $S_{ref} = 34.2$ for simplicity, but with insignificant impact on the results. T_w is the temperature of the source water, taken to be the warmest water of the warm restoring condition, and T_f, the boundary layer freezing point, is taken to be the freezing point at the reference salinity and a depth of 360 m. Temperature and salinity data are taken from the cross-section of the model results at $y = 40$ km, the most complete available datasets for this analysis. Fig. 15 shows that most models produce water masses within the expected

https://doi.org/10.5194/egusphere-2025-1942
Preprint. Discussion started: 24 June 2025

range that is spanned by the restoring conditions and modification by ice shelf melting: T–S properties in all models deviate along the meltwater mixing line from the cold restoring properties (that were used as model initial conditions, blue line) to lower temperatures during the first month of the simulation, confirming the consumption of heat by basal melting of ice at greater pressure in the cold cavity. At the end of the simulation, this cold and saline water mass has been eroded by the warmer Ocean1 forcing, with most models featuring a T–S distribution in the last year (year 20, yellow colours) of the simulation that is bounded by the warm restoring conditions (red line), and the meltwater mixing line originating from the warmest water mass in the domain (black thick line), indicating mixing between these water masses. The absence of significantly colder temperatures than the 100 m melting point in most models at the end of the Ocean1 experiment is consistent with the paradigm of a warm ice shelf cavity circulation, where melt rates are limited by the fluxes across the ice-ocean boundary layer and a significant fraction of the available heat for melting is advected out of the cavity by the buoyancy-driven overturning.

Some models show T–S properties at year 20 "to the right" of the warm restoring conditions (compare yellow and red colours in MITgm-BAS, MITgcm-JPL and NEMO-UKESM1is in Fig. 15). This feature could originate either from remnants of the initial conditions (unlikely, since models are well spun up; Fig. 11), or spurious salinification. The latter is known to have occurred in the imperfect application of the sea level restoring in NEMO-UKESM1is. Additionally, T–S properties "to the left" of the meltwater mixing line (MITgcm-BAS and MITgcm-JPL) indicate spurious freshwater. Both the spuriously fresh and saline features in these two models were found to be caused by the MITgcm advection scheme[2] used, the third-order DST flux limiter option 33 (and can be resolved with alternative advection schemes e.g. the second-order flux limiter option 77). Lower ocean temperatures than the freezing point at 720 m depth (the deepest ice in the domain) may indicate unphysical heat loss in two other models (POP2x and MOM6-SIGMA-ZSTAR, the latter found to be likely caused by diagnostic interpolation errors). T–S properties in ROMS lie below the warm restoring line, likely caused by a combination of the 5 m vertical resolution processed model output not capturing the cold, top boundary layer that is thinner than 5 m (the raw model data has water masses colder and fresher than the warm restoring line, not shown), and also that melting is driven by this cold boundary layer rather than warm restoring conditions, shifting the location of the Gade line. The latter highlights that differences in the water masses that drive melt (either through model differences, boundary layer and mixing choices) create different signatures in T–S space (Fig. 15).

For Ocean2, the water mass evolution reverses (Fig. S4), confirming a transition from a warm cavity into a cold cavity circulation paradigm. However, in some models (MITgcm-BAS-Coupled, MITgcm-JPL and NEMO-CNRS) there is less Ice Shelf Water (water masses colder than the surface freezing point, similar to the dotted line) present in the last year of the Ocean2 experiment compared to the first month of the Ocean1 experiment. These are the same models with a relatively warm interior in Fig. 3. The lack of Ice Shelf Water may be because these Ocean2 models have not yet reached their "cold" steady state (Fig. 3, 11) or a numerical issue, perhaps a consequence of the advection scheme issue noted in the Ocean1 analysis for the MITgcm models. The different ice base geometries between Ocean1 and Ocean2 may also affect the comparison between the first month of Ocean1 and last of Ocean2. The T–S space results indicate that water mass analysis is effective for model verification.

[2]https://mitgcm.readthedocs.io/en/latest/algorithm/adv-schemes.html

https://doi.org/10.5194/egusphere-2025-1942
Preprint. Discussion started: 24 June 2025

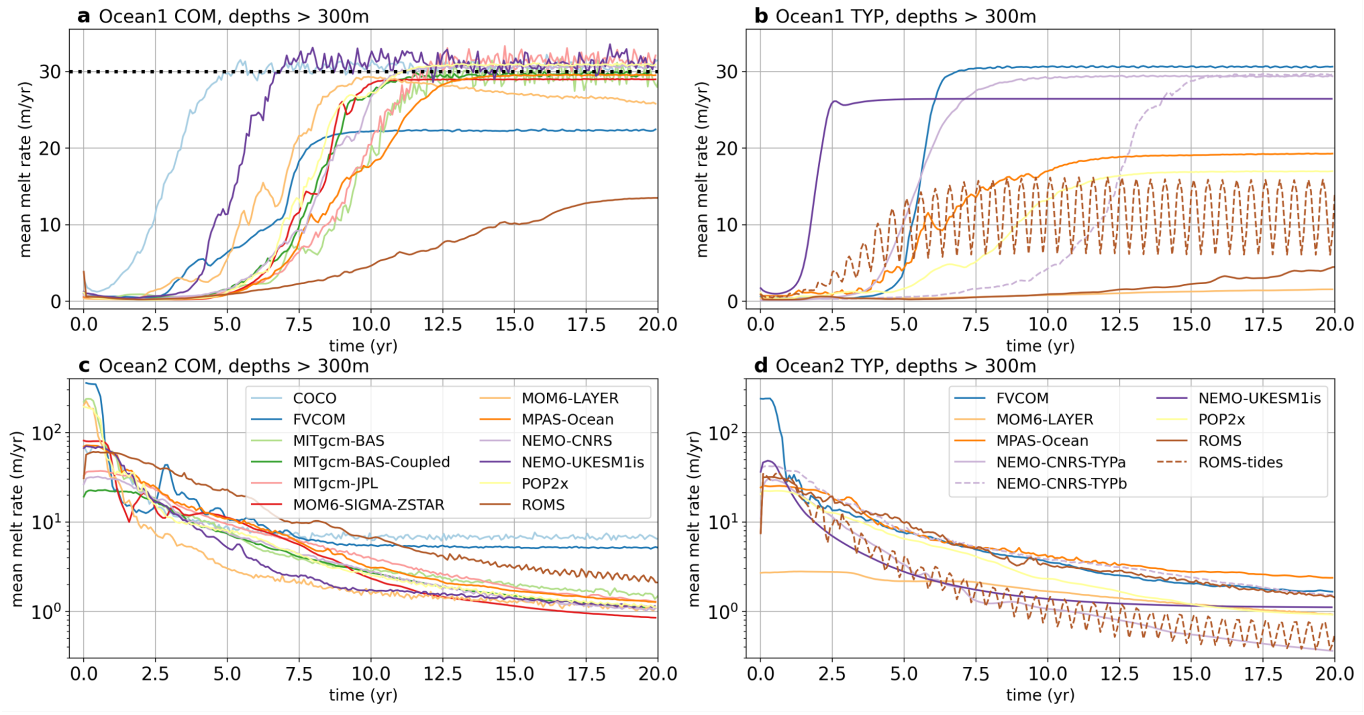

Figure 16. Time series of area-averaged melt rates at ice depths below 300 m for a) Ocean1 COM, b) Ocean1 TYP, c) Ocean2 COM and d) Ocean2 TYP ensembles.

4.5 Typical experiment variability

The TYP set of experiments noted in Sect. 2.7 repeated the geometries and forcing used in Ocean1 and Ocean2 but allowed groups to configure their models as they would choose to do for a typical simulation, relaxing the stricter requirements of resolution, physics and parameter choices required for the COM experiments. COM simulations were the priority in ISOMIP+, and not all groups chose to conduct TYP simulations (Table 2). TYP configuration choices are described in Appendix A.

There are a wide variety of differences between the COM and TYP configurations across the models so it is challenging to find simple explanations when comparing results between the two sets of experiments. It is generally true that a group's TYP model configuration produces less melt in response to the warm ocean forcing than using the idealised COM protocol (Fig. 16a, b). Comparing melt below 300 m, which is the calibration depth used for setting each model's transfer coefficient values in Ocean0, the only model with a higher melt rate in its TYP configuration is FVCOM, which achieves this benchmark with the Ocean1 TYP configuration but not with COM, likely because of the use of different vertical mixing schemes. This lowering of melt rates and a marked increase in the variety of melt responses to warming suggests that the COM protocol may have led to simulations with unrealistically high melting, but succeeded in creating a common ground on which very different models could be compared. Although TYP models generally do not show more melt than COM, there is no consistent picture

https://doi.org/10.5194/egusphere-2025-1942
Preprint. Discussion started: 24 June 2025

when comparing the rate at which the circulation spins up in the Ocean1 experiment. Temporal variability is similar in most TYP models compared to their Ocean1 COM counterparts, except for NEMO-UKESM1is, which has less temporal variability, and the ROMS model equipped with semidiurnal tides, which develops a clear periodic signal (likely showing resonance or aliasing in the monthly output).

There is less variation between COM and TYP in the Ocean2 experiment, with the models generally reducing their melt rates below 300 m at a similar rate (Fig. 16b, d). MPAS-Ocean has a higher final melt rate in TYP than COM in Ocean2 despite having a significantly lower melt rate in TYP compared to COM in Ocean1, and FVCOM shows the opposite behaviour, with more TYP melt in Ocean1 and less in Ocean2. This difference may be associated with changes in the depth at which the buoyant meltwater current separates from the ice. The two TYP variants of NEMO-CNRS achieve the same mean melt rate as each other in Ocean1 but with different timescales, and in Ocean2, after 20 years, they have spun down towards different area-average melt rates. As in COM, few of the Ocean2 TYP models have fully equilibrated melt rates at the end of the 20 years.

Even where TYP configurations produce similar melt rates to COM in response to the boundary forcing, similar melt rates can result from a different balance of physical processes in the cavity (Fig. 17). The strength of the friction velocity varies more widely across the TYP ensemble than COM, indicating a greater variability of circulations in response to the thermal forcing at the boundary (Fig. S14–S15). In several models, the thermal driving term in Ocean1 is higher for the TYP models (Fig. 17), although this does not necessarily translate into higher melt rates since some TYP models will also have changed their transfer coefficient values and vertical mixing. MOM6-LAYER, for instance, produces a much higher thermal driving on the ice shelf in TYP in Ocean1 but has a transfer coefficient that is a factor of ten smaller than used in COM, resulting in the low melt seen for this simulation, coupled with a low friction velocity. Generally, TYP models use smaller transfer coefficients than their COM counterparts (except for the NEMO simulations which tuned their melt rates to 30 m/yr, see Table 2 vs Appendix. A4, A5), and are closer to those suggested by observations (e.g. $C_d^{1/2}\Gamma_T = 1.1 \times 10^{-3}$ suggested by Jenkins et al., 2010, in comparison to an average $C_d^{1/2}\Gamma_T$ of 3.0×10^{-3} across the COM models). However, note that transfer coefficients vary with ice shelf melt regimes and may not be constant in reality (Malyarenko et al., 2020; Rosevear et al., 2022). FVCOM TYP uses a smaller transfer coefficient than its COM counterpart but has a higher melt rate (Fig. 16b), likely explained by its more realistic vertical mixing scheme (Appendix. A1), highlighting the importance of interior mixing choices on melt rates. Additionally, boundary layer temperature profiles of TYP configurations are also diverse and likely related to varying melt rate parameterisation and mixing choices (Fig. S9, S10). Finally, comparing TYP spin-ups, in Fig. 16b, NEMO-CNRS-TYPb is slower to spin up than NEMO-CNRS-TYPa under the Ocean1 forcing. NEMO-CNRS-TYPa has a partial-slip lateral momentum boundary condition, as well as a lower vertical resolution and larger vertical tracer sampling distance (via a Losch (2008)-style scheme), both of which may spin up TYPa faster.

In summary, the TYP experiments demonstrate how the COM experimental protocol moved many models away from their typical behaviour. There is significant variation in the simulated melt, melt drivers and circulation when models use their typical model parameters and resolution. However, untangling mechanisms and causes of model differences amongst the TYP models

https://doi.org/10.5194/egusphere-2025-1942
Preprint. Discussion started: 24 June 2025

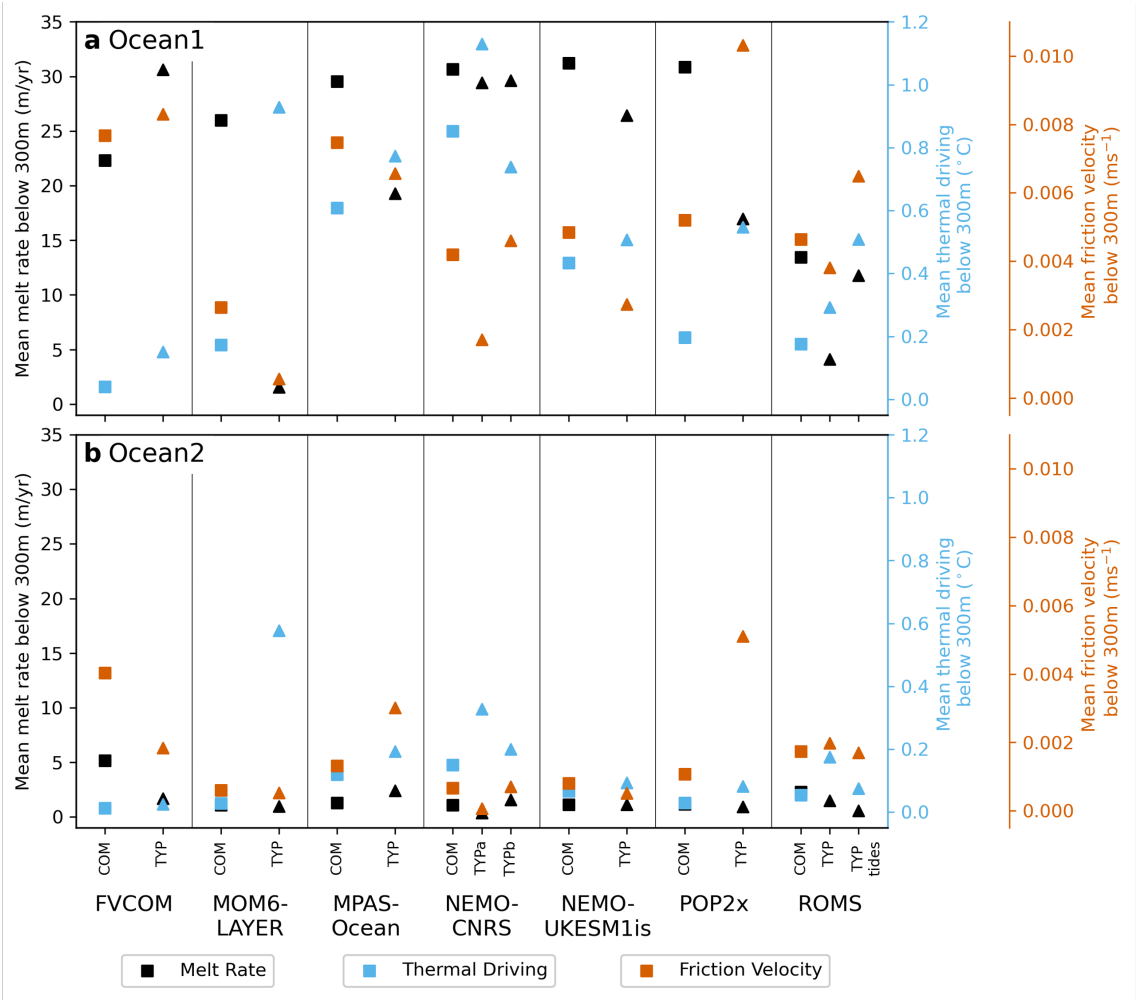

Figure 17. Area-averaged and temporally averaged (over year 20) melt rate ice depths below 300 m (black), thermal driving (blue) and friction velocity (orange) for each model with both a COM (squares) and TYP submission (triangles).

is challenging and emphasises the success of the COM experiments in providing a consistent common ground from which models can be compared.

5 Discussion

The ISOMIP+ project shows that there are a substantial number of ocean models now capable of simulating the ocean circulation in ice shelf cavities and its interactions with the ice shelf. These models have qualitatively similar ocean profiles, melt and circulation when forced with a common, idealised simulation protocol ("COM"). The twelve model configurations submitted to the common Ocean1 and Ocean2 experiments show similar temperature and salinity profiles consistent with the

https://doi.org/10.5194/egusphere-2025-1942
Preprint. Discussion started: 24 June 2025

formation of a fresh, cold meltwater layer (Fig. 2, 3). Melt rates have similar spatial distributions, enhanced at the grounding line where thermal driving is greatest (Fig. 4, 5). All models reproduce the expected buoyancy-driven overturning circulation, and most have similar barotropic circulation within the ice shelf cavity (Fig. 7, 8, 9 10). Models also exhibit similarities during the spin-up, which occurs over a similar ∼5 year time period once initiated (Fig. 11). Melt and circulation strength are linearly proportional in a common relationship for most models, particularly for the Ocean1 experiment (Fig. 12). This common behaviour is not unsurprising given the prescribed, idealised model framework, but it is a positive outcome for the reliability of ice shelf cavity ocean models. Additionally, differences between the warm Ocean1 and cold Ocean2 experiments at steady state can be explained by the different forcing and ice base geometries.

However, there are differences between the models across several diagnostics. Melt rate patterns for Ocean1 vary (Fig. 4, 6), some affected by the vertical coordinate and modifications to geometry. Variation in melt rate spatial distributions, particularly near the grounding line and side walls, has implications for ice sheet evolution in coupled ocean–ice sheet models to be explored in the complementary MISOMIP1 model analysis (Seroussi et al. *in prep*). Overturning and barotropic streamfunctions also indicate differences in the cavity circulation patterns (Fig. 7, 10). Models also differ significantly in the ice–ocean boundary layer. ISOMIP+ COM models have their transfer coefficients tuned to achieve a given melt rate at depth, resulting in an order of magnitude spread of their values (Table 2). Boundary layer temperature and salinity (Fig. 13, S2), as well as thermal driving and friction velocity (Fig. 14), vary between models. These differences occur mainly between groups of models with different vertical coordinates, highlighting the sensitivity of ice shelf basal melt and circulation to the choice of the vertical coordinates (Gwyther et al., 2020) and emphasising the challenges in parameterising and modelling boundary layer processes under ice shelves in ocean models.

There are also outliers in certain diagnostics. The COCO setup used in ISOMIP+ has an anomalously strong circulation, possibly related to spurious currents from the implementation of the sponge boundary. The NEMO-UKESM1is setup used here has a known surface cooling error that results in a cooler interior. The MITgcm models used here have anomalously fresh meltwater associated with the advection scheme (Fig. 15, S4), and the transfer coefficients of MITgcm-BAS appear to be inconsistent (Fig. S3). However, these differences are likely associated with the imperfect implementation of the idealised model protocol rather than fundamental issues with the models. Outliers worth highlighting are the low melt rates in the ROMS and FVCOM model submissions (Fig. 11), which could not achieve the target melt rate of $30\,\mathrm{m\,yr^{-1}}$ even with large transfer coefficients (Fig. 16a). The $30\,\mathrm{m\,yr^{-1}}$ target was contrived based on a z-level model and may not represent what melt the Ocean0 domain and forcing would create in reality, particularly given the other idealised model assumptions made, such as the low internal vertical mixing – a limitation of the experimental setup. The ROMS and FVCOM results highlight the effect of different vertical coordinates, meltwater forcing sampling and flux distribution schemes on simulating ice shelf basal melting.

Low melt rates in ROMS and FVCOM can be explained by the high vertical resolution of their terrain-following coordinates, leading to relatively thin upper cell thicknesses. Meltwater fluxes are distributed into this upper cell and can only be mixed downwards by the explicit vertical mixing; most other models apply a Losch (2008)-style scheme, which induces an effective mixing over a chosen depth that is typically deeper than the s-coordinate top cell thickness. The paradigm used by ROMS and FVCOM thus likely leads to reduced vertical mixing of meltwater fluxes and a thin, fresh meltwater layer (Fig. 13),

https://doi.org/10.5194/egusphere-2025-1942
Preprint. Discussion started: 24 June 2025

which is further emphasised by the prescribed low vertical mixing coefficients in the COM setup. Consequently, the sampling of temperature and salinity properties for the melt parameterisation will be more influenced by the colder meltwater fluxes leading to reduced thermal driving (Gwyther et al., 2020). Gwyther et al. (2020) demonstrate this effect using an ISOMIP+ Ocean0 experiment with a modified version of ROMS that effectively simulated a Losch (2008)-style scheme and find that melt rates increase with effective mixing depth (beyond $30\,\mathrm{m\,yr^{-1}}$). Scott et al. (2023) also suggest that melt rates converge with higher vertical resolution and low vertical mixing. These studies suggest that models with higher resolution near the ice-ocean boundary, such as terrain-following and hybrid coordinate models, better represent the ice-ocean boundary layer with regard to numerical convergence (given a mixing and/or meltwater distribution scheme). At the same time, the results from the COM and TYP experiments highlight the sensitivity of the simulated melt rates and ice-ocean boundary layer structure to the integration of the applied basal melt parameterisation and the model's interior vertical mixing parameterisation.

The analysis of the TYP models (Sect. 4.5) highlights the variability in melt rates created by modifying model parameters. Since multiple changes may have been made between COM and TYP configurations, it is difficult to identify a causal link between specific parameter changes and the resultant ice shelf melt and circulation. However, it is clear that there is a complex relationship between melt rate, the spin-up of melt and circulation (Fig. 16), and melt rate drivers of friction velocity and thermal driving (Fig. 17), and that models typically used for realistic test cases vary significantly when compared in the ISOMIP+ idealised framework.

The model variability seen in the ISOMIP+ ensemble may also be influenced by the idealised model framework. Ocean models used to simulate realistic geographic domains may be constrained to prescribed atmospheric forcings or tuned to achieve an ocean and ice state similar to existing observations (noting different models may need different model parameters to achieve the same state, unlike the prescriptive COM protocol here: the comparison between TYP and COM experiments demonstrates the large impact of model choices). Additionally, differences between ISOMIP+ models may be enhanced by the idealised setup. For example, the open-ocean gyres that differ greatly between models are likely an artifact of the idealised, sponge-forced model setup that is highly sensitive to geometry choices (Zhao et al., 2022). The variation of models in this idealised framework, particularly in the ice shelf–ocean boundary layer, highlights that conclusions made with one idealised ocean model may not be directly applicable to other ocean models. This may be an important consideration for melt parameterisation development, particularly with machine learning methods.

Though there are clear differences between the ice shelf–ocean boundary layer and melt rates across models, there are methods to reconcile these. By calibrating the depth over which temperature, salinity and velocities are sampled in the three-equation melt parameterisation and the distance over which freshwater or a virtual salt flux is distributed, similar melt rates can be achieved with different vertical coordinates and resolution (Gwyther et al., 2020). Melt rates can also converge as the vertical resolution is enhanced (Scott et al., 2023). Models will likely require tuning and development of the melt parameterisation in future Antarctic ice shelf simulations to achieve melt rates and ice shelf cavity conditions consistent with *in situ* observations.

Finally, the idealised framework of ISOMIP+ presents difficulties in generalising the model intercomparison results across realistic Antarctic ice shelves or assessing biases compared to observations. For example, the different ice geometries of the ISOMIP+ experiments are highly idealised compared to real Antarctic ice shelves. Realistic ice shelf–ocean model intercom-

https://doi.org/10.5194/egusphere-2025-1942
Preprint. Discussion started: 24 June 2025

parison projects such as RISE (Galton-Fenzi et al., in review) and MISOMIP2 (De Rydt et al., 2024) will provide the next assessments of our ice sheet-ocean modelling capabilities and guide future model development.

6 Conclusions

We have presented the results of the second Ice Shelf–Ocean Model Intercomparison Project, ISOMIP+. Twelve model configurations (eight independent ocean models) in a common model setup were submitted across a tuning and two forcing experiments. Nine model configurations were also submitted in a more flexible, typical category. Through the common, idealised modelling framework, we demonstrate the consistency in simulated basal melt rate and ice shelf cavity circulation across the models and a shared relationship between melt rate and circulation. However, we highlight the differences in boundary layer characteristics between models and the order of magnitude spread in transfer coefficients required to parameterise a common melt rate. We find that many differences in the model results can be explained by the use of different vertical coordinates. This sensitivity highlights the need for improved representation of the ice shelf–ocean boundary layer processes and their integration with the model-specific interior vertical mixing schemes, requiring further research and direct observations of the boundary layer. When constraints on model parameters are relaxed, the variation in boundary layers, melt rate and cavity circulation is further enhanced. However, this variation may be enhanced by the idealised nature of the ISOMIP+ setup, where not all the models could follow the exact idealised protocol. Future work will compare models in realistic ice shelf–ocean configurations to assess the state of ice sheet–ocean modelling and guide model development for improved Antarctic Ice Sheet, climate and sea level projections.

Code and data availability. The code used to prepare the figures is available at https://github.com/misomip/isomip-plus. Submitted model data and metadata (PDF information sheets) will be made available on the platform Open Science Framework (https://osf.io/).

Appendix A: Typical model configurations (TYP)

Here, we outline the changes made to develop the TYP configurations from the COM experiments for each model. Where details are missing, models use the COM parameters (Sect. 3).

A1 FVCOM

The horizontal resolution in the FVCOM TYP submission is increased in regions of steeply sloping topography (ranging from 200 m-2000 m). Mixing schemes that are typically used in more realistic applications were also employed. Vertical mixing uses the Mellor and Yamada level 2.5 turbulent closure model (Mellor and Yamada, 1982; Galperin et al., 1988) with background viscosity and diffusivity set to $10^{-5}\mathrm{m}^2\mathrm{s}^{-1}$. Horizontal mixing uses the Smagorinsky eddy parameterisation (Smagorinsky,

https://doi.org/10.5194/egusphere-2025-1942
Preprint. Discussion started: 24 June 2025

1963), with the constant used in the parameterisation being 0.1. Alternative transfer coefficients of $\Gamma_T = 0.06$ and $\Gamma_S = 1.7 \times 10^{-3}$ are also used.

A2 MOM6-LAYER

The MOM6-LAYER TYP submission is similar to MOM6-LAYER COM, but has a higher vertical resolution with 72 isopycnal layers. The ice geometry is also modified to have a minimum ocean thickness of 40 m. The Holland and Jenkins (1999) basal melt parameterisation is used with the McPhee (1981) stability parameter. The experiments also included frazil ice formation, in which seawater is artificially warmed to its freezing point when the temperature falls below that threshold.

A3 MPAS-Ocean

The MPAS-Ocean TYP submission has a coarser horizontal resolution than COM, of 5 km, which is close to the highest resolution that MPAS-Ocean is typically run at in the Energy Exascale Earth System Model (E3SM). Horizontal momentum is mixed with a biharmonic scheme, with $\nu_H = -1.0 \times 10^9 \mathrm{m}^4\mathrm{s}^{-1}$, and tracers were not mixed horizontally. Vertical mixing is parameterised by the Community Vertical Mixing library (CVMix Griffies et al., 2015) with background vertical diffusion and shear-based mixing via the K-Profile Parameterization (Large et al., 1994) (parameter values in supplementary model description documents). Output is presented as snapshots rather than monthly output due to constraints at the time of production. A nonlinear density equation of state from Jackett and Mcdougall (1995) is used, and a nonlinear freezing equation of state (a least-squares fit to TEOS-10, Millero et al. 2008, over salinities between 20 and 40 and pressures between 0 and 2×10^7 Pa) is also used with a salinity–pressure cross-term ($\lambda_1 = -5.64 \times 10^{-2}\,^\circ\mathrm{C}$, $\lambda_2 = 6.22 \times 10^{-2}\,^\circ\mathrm{C}$, $\lambda_3 = -7.43 \times 10^{-8}\,^\circ\mathrm{C\ Pa}^{-1}$, $\lambda_4 = -1.74 \times 10^{-10}\,^\circ\mathrm{C\ Pa}^{-1}$). The transfer coefficients from Jenkins et al. (2010) were used; $\Gamma_T = 0.011$ and $\Gamma_S = 3.1 \times 10^{-4}$. The tidal velocity is increased to $0.05\,\mathrm{ms}^{-1}$ and bottom drag coefficient decreased to 1×10^{-3}.

A4 NEMO-CNRS

There are two NEMO-CNRS submissions, TYPa and TYPb.

TYPa has a 2.4 km resolution and 75 vertical levels ranging from 1 m at the surface to ∼100 m at 1000 m depth. This grid represents the 1/12° NEMO configuration used for the Amundsen Sea in Jourdain et al. (2017). Compared to the NEMO-CNRS COM configuration, TYPa uses the EOS80 equation of state (ICES, SCOR, and IAPSO, 1981), a 100 times stronger vertical mixing in unstable conditions, a TKE vertical mixing scheme in stable conditions (Madec et al., 2019), a 30 m Losch (2008)-style layer over which temperatures, salinities and velocities are averaged to compute melt, and lateral advection and diffusion as in Jourdain et al. (2017), with partial slip as lateral boundary condition for momentum. The prescribed tidal velocity is set to zero. The transfer coefficients are modified to $\Gamma_T = 4.8 \times 10^{-2}$ and $\Gamma_S = 1.37143 \times 10^{-3}$, while the top interface drag coefficient is $C_D = 1.0 \times 10^{-3}$.

https://doi.org/10.5194/egusphere-2025-1942
Preprint. Discussion started: 24 June 2025

TYPb is a more idealised experiment, similar to the COM experiment, but run at 1 km resolution and with a different representation of vertical mixing: the TKE scheme in stable conditions and a 100 times stronger vertical mixing in unstable conditions. The Losch (2008)-style layer over which temperatures, salinities and velocities are averaged to compute melt is also thinner, with 10 m thickness. Although not identical, this experiment is similar to the TYP-1km experiment described in Favier et al. (2019). Transfer coefficients are modified to $\Gamma_T = 2.63 \times 10^{-2}$ and $\Gamma_S = 7.51429 \times 10^{-4}$.

A5 NEMO-UKESM1is

The NEMO-UKESM1is TYP setup is very similar to UKESMis simulation (Smith et al., 2021). The major difference with COM is the use of a coarse grid equivalent to a sector of the eORCA025 global grid used in GO7 (Storkey et al., 2018). Horizontal diffusivity of momentum is biharmonic and along geopotentials, horizontal tracer diffusivity is increased to $\kappa_H = 260\,\mathrm{m^2 s^{-1}}$, a weaker vertical stable mixing is used ($\nu_{\text{stab}} = 1 \times 10^{-4}\,\mathrm{m^2 s^{-1}}$, $\kappa_{\text{stab}} = 1 \times 10^{-5}\,\mathrm{m^2 s^{-1}}$), a 100 times stronger vertical mixing ($\kappa_{\text{unstab}} = 10\,\mathrm{m^2 s^{-1}}$) is used in unstable conditions, the convective vertical viscosity ν_{stab} is set to zero, and the TEOS-10 equation of state (IOC et al., 2010; Roquet et al., 2015) is used. The lower bottom drag coefficient is decreased to 1.0×10^{-3}, and a diffusive bottom boundary layer parameterisation is used. As in COM, the evaporative flux that maintains sea level was incorrectly allowed to affect the salinity of the remaining surface water. The Γ_T and Γ_S coefficients were tuned to achieve the COM target melt rate in Ocean0, and are $\Gamma_T = 0.06$, $\Gamma_S = 0.001714$.

A6 POP2x

The POP2x TYP submission has a different model resolution compared to its COM counterpart of 4 km in the horizontal and 48 layers in the vertical, with increasing thickness with depth from 10 m at the surface to 40 m at the bottom. A thicker layer of 30 m is used to sample temperature and salinity for the melt parameterisation as well as distribute the melt fluxes, and the transfer and drag coefficients from Jenkins et al. (2010), $\Gamma_T = 0.011$, $\Gamma_S = 3.1 \times 10^{-4}$ and $C_{D,\text{top}} = 9.7 \times 10^{-3}$ were used, with bottom drag reduced to $C_{D,\text{bottom}} = 1 \times 10^{-3}$. The configuration uses a nonlinear density equation of state from McDougall et al. (2003) and a modified linear freezing equation of state ($\lambda_1 = -5.89 \times 10^{-2}\,^\circ\mathrm{C}$, $\lambda_2 = 0.153^\circ\mathrm{C}$, $\lambda_3 = -8.04 \times 10^{-8}\,^\circ\mathrm{C\ Pa^{-1}}$). Vertical mixing is parameterised with the Pacanowski and Philander (1981) convective adjustment scheme based on the Richardson number with $\nu_b = 1 \times 10^{-3}\,\mathrm{m^2 s^{-1}}$, $\kappa_b = 1 \times 10^{-4}\,\mathrm{m^2\,s^{-1}}$ and $\nu_0 = 5 \times 10^{-3}\,\mathrm{m^2\,s^{-1}}$. The unstable enhanced vertical mixing is increased ten-fold to $1\,\mathrm{m^2 s^{-1}}$. Biharmonic horizontal mixing is used with $\nu_H = -7.0 \times 10^9\,\mathrm{m^4\,s^{-1}}$. The tidal velocity is increased to $0.05\,\mathrm{m\,s^{-1}}$.

A7 ROMS

The two ROMS TYP configurations use different mixing schemes to COM. Vertical diffusivity and viscosity is implemented through the K-Profile Parameterisation (KPP, Large et al., 1994) with parameters $\nu_{\text{stab}} = 1 \times 10^{-4}\mathrm{m^2 s^{-1}}$ and $\kappa_{\text{stab}} = 1 \times 10^{-6}\mathrm{m^2 s^{-1}}$ and unstable mixing coefficients are calculated by KPP. Horizontal harmonic diffusion for tracers is set to zero. Horizontal mixing of momentum and tracers are both scaled by grid size, and momentum diffusion is computed along

https://doi.org/10.5194/egusphere-2025-1942
Preprint. Discussion started: 24 June 2025

sigma surfaces rather than geopotential levels. A nonlinear density equation of state is used (Jackett and Mcdougall, 1995), with coefficients available in the model description PDF. Turbulent exchange velocities follow McPhee et al. (1987) rather than constant transfer coefficients. The linear freezing equation of state is also modified slightly ($\lambda_1 = -5.7 \times 10^{-2}\,^\circ\mathrm{C}$, $\lambda_2 = -0.0939 \times 10^{-2}\,^\circ\mathrm{C}$, $\lambda_3 = -7.61 \times 10^{-4}\,^\circ\mathrm{C m^{-1}}$). The ROMS tides run also includes a forced tide with a 12 hour period, designed to emulate the S2 tide. This is achieved by forcing the u-momentum at the x=800 km boundary towards a barotropic sinusoidal profile with 0.5 $\mathrm{ms^{-1}}$ amplitude.

Author contributions. CKY led the manuscript preparation and analysis. XSAD led the project planning, model submission collection, data verification and initial analysis. Visualisations were developed by CKY, XSAD, CYSB, DEG, TH, NCJ, GM, AKM, RSS and QZ. The first draft was written by CKY, XSAD, MSD, BKG, DEG, DMH, TH, JRJ, NCJ, KK, PM, GM, AKM, YN, RSS and QZ with initial review and editing by PRH, JDR and OS, and further review and editing by all authors. All authors except CKY and AKM contributed to model submissions and/or ISOMIP+ project planning.

Competing interests. Some authors are members of the editorial board of The Cryosphere.

Acknowledgements. Support for the preparation of this work was provided by the New York University Abu Dhabi Research Institute, the National Science Foundation Antarctic Integrated System Science Program, the NASA Cryospheric Program, and the WCRP CliC. RSS, CYSB, PRH and PM are grateful to Antony Siahaan for assistance in running the experiments presented here.

CKY acknowledges support from an Australian Government Research Training Program Scholarship and the Consortium for Ocean Sea Ice Modelling in Australia (COSIMA). CKY and AKM were supported by the Australian Research Council (ARC) Special Research Initiative, the Australian Centre for Excellence in Antarctic Science (SR200100008) and the ARC Discovery Projects DP190100494 and DP250100759. Support for XSAD was provided through the Scientific Discovery through Advanced Computing (SciDAC) program funded by the US Department of Energy (DOE), Office of Science, Advanced Scientific Computing Research and Biological and Environmental Research Programs. DEG was supported by the Australian Research Council Discovery Project DP22010252. QZ and TH received financial support from the Research Council of Norway under projects 295075, 343397 and 332635. YN was supported by the funds from Grants-in-Aid for Scientific Research of the Japanese Ministry of Education, Culture, Sports, Science and Technology (24K15256,24H02341). Additionally, YN and DM were supported by the NASA Sea Level Change Team (80NSSC24K1532). The FVCOM simulations are supported by Sigma2 HPC, Norway, project NN9824K. RSS was supported by the UKESM project, UK Natural Environment Research Council national capability grant number NE/N017951/1. The NEMO-UKESM1is computational resources were provided by the ARCHER UK National Supercomputing Service. CYSB was supported by the UK Natural Environment Research Council (NERC) through the Filchner Ice Shelf System project (NE/L013770/1). NCJ was supported by the French National Research Agency (ANR) through the TROIS-AS (ANR-15-CE01-0005-01) and SUMER (ANR-12-BS06-0018) projects. NEMO-CNRS simulations were run at CINES, with computing time provided by GENCI. PM has received funding from Agence Nationale de la Recherche - France 2030 as part of the PEPR TRACCS programme under grant number ANR-22-EXTR-0010. KK was supported by JSPS KEKENHI Grants JP24K15281. This material is also

https://doi.org/10.5194/egusphere-2025-1942
Preprint. Discussion started: 24 June 2025

based upon work supported by the National Center for Atmospheric Research (NCAR), which is a major facility sponsored by the NSF under cooperative agreement no. 1852977 (GM). Computing resources (DOI:10.5065/D6RX99HX) for MOM6 simulations were provided by the Climate Simulation Laboratory at NCAR's Computational and Information Systems Laboratory, sponsored by the National Science Foundation and other agencies. This study was also supported by an award NA23OAR4320198 from the National Oceanic and Atmospheric Administration, U.S. Department of Commerce (AA and OS) and a National Oceanic and Atmospheric Administration Climate Process Team grant NA13OAR4310097 (AS). The statements, findings, conclusions and recommendations are those of the authors and do not necessarily reflect the views of the National Oceanic and Atmospheric Administration, or the U.S. Department of Commerce.

https://doi.org/10.5194/egusphere-2025-1942
Preprint. Discussion started: 24 June 2025

References

Adcroft, A. and Campin, J.-M.: Rescaled height coordinates for accurate representation of free-surface flows in ocean circulation models, Ocean Modelling, 7, 269–284, https://doi.org/10.1016/j.ocemod.2003.09.003, 2004.

Adcroft, A., Hill, C., and Marshall, J.: Representation of topography by shaved cells in a height coordinate ocean model, Monthly Weather Review, 125, 2293–2315, https://doi.org/10.1175/1520-0493(1997)125<2293:ROTBSC>2.0.CO;2, 1997.

Adcroft, A., Anderson, W., Balaji, V., Blanton, C., Bushuk, M., Dufour, C. O., Dunne, J. P., Griffies, S. M., Hallberg, R., Harrison, M. J., et al.: The GFDL global ocean and sea ice model OM4. 0: Model description and simulation features, J. Adv. Model. Earth Sys., 11, 3167–3211, https://doi.org/10.1029/2019MS001726, 2019.

Arakawa, A.: Computational design for long-term numerical integration of the equations of fluid motion: Two-dimensional incompressible flow. Part I, Journal of Computational Physics, 1, 119–143, https://doi.org/https://doi.org/10.1016/0021-9991(66)90015-5, 1966.

Asay-Davis, X. S., Cornford, S. L., Durand, G., Galton-Fenzi, B. K., Gladstone, R. M., Gudmundsson, G. H., Hattermann, T., Holland, D. M., Holland, D., Holland, P. R., et al.: Experimental design for three interrelated marine ice sheet and ocean model intercomparison projects: MISMIP v. 3 (MISMIP+), ISOMIP v. 2 (ISOMIP+) and MISOMIP v. 1 (MISOMIP1), Geoscientific Model Development, 9, 2471–2497, https://doi.org/10.5194/gmd-9-2471-2016, 2016.

Asay-Davis, X. S., Jourdain, N. C., and Nakayama, Y.: Developments in simulating and parameterizing interactions between the Southern Ocean and the Antarctic ice sheet, Current Climate Change Reports, 3, 316–329, https://doi.org/10.1007/s40641-017-0071-0, 2017.

Barnier, B., Madec, G., Penduff, T., Molines, J.-M., Treguier, A.-M., Le Sommer, J., Beckmann, A., Biastoch, A., Böning, C., Dengg, J., et al.: Impact of partial steps and momentum advection schemes in a global ocean circulation model at eddy-permitting resolution, Ocean Dynam., 56, 543, https://doi.org/10.1007/s10236-006-0082-1, 2006.

Beckmann, A. and Haidvogel, D. B.: Numerical simulation of flow around a tall isolated seamount. Part I: Problem formulation and model accuracy, Journal of Physical Oceanography, 23, 1736–1753, https://doi.org/10.1175/1520-0485(1993)023<1736:NSOFAA>2.0.CO;2, 2003.

Bett, D. T., Bradley, A. T., Williams, C. R., Holland, P. R., Arthern, R. J., and Goldberg, D. N.: Coupled ice–ocean interactions during future retreat of West Antarctic ice streams in the Amundsen Sea sector, The Cryosphere, 18, 2653–2675, https://doi.org/10.5194/tc-18-2653-2024, 2024.

Bronselaer, B., Winton, M., Griffies, S. M., Hurlin, W. J., Rodgers, K. B., Sergienko, O. V., Stouffer, R. J., and Russell, J. L.: Change in future climate due to Antarctic meltwater, Nature, 564, 53–58, https://doi.org/10.1038/s41586-018-0712-z, 2018.

Buissou, B., Burgard, C., and Jourdain, N. C.: Parameterising ocean-induced melt of an idealised Antarctic ice shelf using deep learning, in: ECCOMAS Congress 2022 - 8th European Congress on Computational Methods in Applied Sciences and Engineering, https://www.scipedia.com/public/Bouissou_et_al_2022a, 2022.

Burgard, C., Jourdain, N. C., Reese, R., Jenkins, A., and Mathiot, P.: An assessment of basal melt parameterisations for Antarctic ice shelves, The Cryosphere, 16, 4931–4975, https://doi.org/10.5194/tc-16-4931-2022, 2022.

Campin, J.-M., Marshall, J., and Ferreira, D.: Sea ice–ocean coupling using a rescaled vertical coordinate z_*, Ocean Modelling, 24, 1–14, https://doi.org/https://doi.org/10.1016/j.ocemod.2008.05.005, 2008.

Cessi, P. and Young, W.: Some unexpected consequences of the interaction between convective adjustment and horizontal diffusion, Physica D: Nonlinear Phenomena, 98, 287–300, https://doi.org/10.1016/0167-2789(96)00118-2, 1996.

https://doi.org/10.5194/egusphere-2025-1942
Preprint. Discussion started: 24 June 2025

Chen, C., Liu, H., and Beardsley, R. C.: An unstructured, finite-volume, three-dimensional, primitive equation ocean model: application to coastal ocean and estuaries., J. Atmos. Ocean. Technol., 20, 159–186, https://doi.org/10.1175/1520-0426(2003)020<0159:AUGFVT>2.0.CO;2, 2003.

Christianson, K., Bushuk, M., Dutrieux, P., Parizek, B. R., Joughin, I. R., Alley, R. B., Shean, D. E., Abrahamsen, E. P., Anandakrishnan, S., Heywood, K. J., et al.: Sensitivity of Pine Island Glacier to observed ocean forcing, Geophysical Research Letters, 43, 10–817, https://doi.org/10.1002/2016GL070500., 2016.

Cornford, S. L., Martin, D. F., Graves, D. T., Ranken, D. F., Le Brocq, A. M., Gladstone, R. M., Payne, A. J., Ng, E. G., and Lipscomb, W. H.: Adaptive mesh, finite volume modeling of marine ice sheets, Journal of Computational Physics, 232, 529–549, https://doi.org/10.1016/j.jcp.2012.08.037, 2013.

Cornford, S. L., Seroussi, H., Asay-Davis, X. S., Gudmundsson, G. H., Arthern, R., Borstad, C., Christmann, J., Dias dos Santos, T., Feldmann, J., Goldberg, D., Hoffman, M. J., Humbert, A., Kleiner, T., Leguy, G., Lipscomb, W. H., Merino, N., Durand, G., Morlighem, M., Pollard, D., Rückamp, M., Williams, C. R., and Yu, H.: Results of the third Marine Ice Sheet Model Intercomparison Project (MISMIP+), The Cryosphere, 14, 2283–2301, https://doi.org/10.5194/tc-14-2283-2020, 2020.

De Rydt, J. and Naughten, K.: Geometric amplification and suppression of ice-shelf basal melt in West Antarctica, The Cryosphere, 18, 1863–1888, https://doi.org/10.5194/tc-18-1863-2024, 2024.

De Rydt, J., Jourdain, N. C., Nakayama, Y., van Caspel, M., Timmermann, R., Mathiot, P., Asay-Davis, X. S., Seroussi, H., Dutrieux, P., Galton-Fenzi, B., Holland, D., and Reese, R.: Experimental design for the Marine Ice Sheet–Ocean Model Intercomparison Project – phase 2 (MISOMIP2), Geoscientific Model Development, 17, 7105–7139, https://doi.org/10.5194/gmd-17-7105-2024, 2024.

Dinniman, M. S., Klinck, J. M., and Smith Jr, W. O.: Influence of sea ice cover and icebergs on circulation and water mass formation in a numerical circulation model of the Ross Sea, Antarctica, Journal of Geophysical Research: Oceans, 112, 1–13, https://doi.org/10.1029/2006JC004036, 2007.

Dinniman, M. S., Asay-Davis, X. S., Galton-Fenzi, B. K., Holland, P. R., Jenkins, A., and Timmermann, R.: Modeling ice shelf/ocean interaction in Antarctica: A review, Oceanography, 29, 144–153, https://doi.org/10.5670/oceanog.2016.106, 2016.

Durand, G., van den Broeke, M. R., Le Cozannet, G., Edwards, T. L., Holland, P. R., Jourdain, N. C., Marzeion, B., Mottram, R., Nicholls, R. J., Pattyn, F., et al.: Sea-level rise: From global perspectives to local services, Frontiers in Marine Science, 8, 709 595, 2022.

Dutrieux, P., De Rydt, J., Jenkins, A., Holland, P. R., Ha, H. K., Lee, S. H., Steig, E. J., Ding, Q., Abrahamsen, E. P., and Schröder, M.: Strong sensitivity of Pine Island ice-shelf melting to climatic variability, Science, 343, 174–178, https://doi.org/10.1126/science.1244341, 2014.

Favier, L., Durand, G., Cornford, S. L., Gudmundsson, G. H., Gagliardini, O., Gillet-Chaulet, F., Zwinger, T., Payne, A., and Le Brocq, A. M.: Retreat of Pine Island Glacier controlled by marine ice-sheet instability, Nature Climate Change, 4, 117–121, https://doi.org/10.1038/nclimate2094, 2014.

Favier, L., Jourdain, N. C., Jenkins, A., Merino, N., Durand, G., Gagliardini, O., Gillet-Chaulet, F., and Mathiot, P.: Assessment of sub-shelf melting parameterisations using the ocean–ice-sheet coupled model NEMO (v3. 6)–Elmer/Ice (v8. 3), Geoscientific Model Development, 12, 2255–2283, https://doi.org/10.5194/gmd-12-2255-2019, 2019.

Finucane, G. and Stewart, A.: A predictive theory for heat transport into ice shelf cavities, Geophysical Research Letters, 51, e2024GL108 196, https://doi.org/10.1029/2024GL108196, 2024.

Gade, H. G.: Melting of ice in sea water: A primitive model with application to the Antarctic ice shelf and icebergs, Journal of Physical Oceanography, 9, 189–198, https://doi.org/10.1175/1520-0485(1979)009<0189:MOIISW>2.0.CO;2, 1979.

https://doi.org/10.5194/egusphere-2025-1942
Preprint. Discussion started: 24 June 2025

Galperin, B., Kantha, L., Hassid, S., and Rosati, A.: A quasi-equilibrium turbulent energy model for geophysical flows, Journal of the Atmospheric Sciences, 45, https://doi.org/10.1175/1520-0469(1988)045<0055:AQETEM>2.0.CO;2, 1988.

Galton-Fenzi, B., Hunter, J., Coleman, R., Marsland, S., and Warner, R.: Modeling the basal melting and marine ice accretion of the Amery Ice Shelf, Journal of Geophysical Research: Oceans, 117, https://doi.org/10.1029/2012JC008214, 2012.

Galton-Fenzi, B., Fricker, H. A., Bassis, J. N., Crawford, A. J., Gomez, N., and Schoof, C.: The Antarctic Ice Sheet and sea level: contemporary changes and future projections, in: Antarctica and the Earth System, edited by Meredith, M., Melbourne-Thomas, J., Raphael, M., and Garabato, A. N., Taylor & Francis Group, https://doi.org/10.4324/9781003406471-7, 2025.

Galton-Fenzi, B. K.: Modelling ice-shelf/ocean interaction, Ph.D. thesis, University of Tasmania, https://doi.org/10.25959/23233199.v1, 2009.

Galton-Fenzi, B. K., Porter-Smith, R., Cook, S., Cougnon, E., Gwyther, D. E., Huneke, W. G. C., Rosevear, M. G., Asay-Davis, X., Boeira Dias, F., Dinniman, M. S., Holland, D., Kusahara, K., Naughten, K. A., Nicholls, K. W., Pelletier, C., Richter, O., Seroussi, H. L., and Timmermann, R.: Realistic ice-shelf/ocean state estimates (RISE) of Antarctic basal melting and drivers, EGUsphere, 2025, 1–27, https://doi.org/10.5194/egusphere-2024-4047, in review.

Goldberg, D., Snow, K., Holland, P., Jordan, J., Campin, J.-M., Heimbach, P., Arthern, R., and Jenkins, A.: Representing grounding line migration in synchronous coupling between a marine ice sheet model and a z-coordinate ocean model, Ocean Modelling, 125, 45–60, https://doi.org/10.1016/j.ocemod.2018.03.005, 2018.

Griffies, S., Levy, M., Adcroft, A., Danabasoglu, G., Hallberg, R., Jacobsen, D., Large, W., and Ringler, T.: Theory and Numerics of the Community Ocean Vertical Mixing (CVMix) Project, Technical Report, 2015.

Grosfeld, K., Gerdes, R., and Determann, J.: Thermohaline circulation and interaction between ice shelf cavities and the adjacent open ocean, Journal of Geophysical Research: Oceans, 102, 15 595–15 610, https://doi.org/10.1029/97JC00891, 1997.

Gwyther, D. E., Galton-Fenzi, B. K., Dinniman, M. S., Roberts, J. L., and Hunter, J. R.: The Effect of Basal Friction on Melting and Freezing in Ice Shelf–Ocean Models, Ocean Modelling, 95, 38–52, https://doi.org/10.1016/j.ocemod.2015.09.004, 2015.

Gwyther, D. E., Cougnon, E. A., Galton-Fenzi, B. K., Roberts, J. L., Hunter, J. R., and Dinniman, M. S.: Modelling the response of ice shelf basal melting to different ocean cavity environmental regimes, Annals of Glaciology, 57, 131–141, https://doi.org/10.1017/aog.2016.31, 2016.

Gwyther, D. E., Kusahara, K., Asay-Davis, X. S., Dinniman, M. S., and Galton-Fenzi, B. K.: Vertical processes and resolution impact ice shelf basal melting: A multi-model study, Ocean Modelling, 147, 101 569, https://doi.org/10.1016/j.ocemod.2020.101569, 2020.

Hallberg, R.: The ability of large-scale ocean models to accept parameterizations of boundary mixing, and a description of a refined bulk mixed-layer model, in: Proceedings of the 2003 Aha Hulikoa Hawaiian Winter Workshop, pp. 187–203, 2003.

Haney, R. L.: On the Pressure Gradient Force over Steep Topography in Sigma Coordinate Ocean Models, Journal of Physical Oceanography, 21, 610–619, https://doi.org/10.1175/1520-0485(1991)021<0610:OTPGFO>2.0.CO;2, 1991.

Hasumi, H.: CCSR Ocean Component Model (COCO) Version 4.0. CCSR report No. 25, Tech. rep., https://ccsr.aori.u-tokyo.ac.jp/~hasumi/COCO/coco4.pdf, 2006.

Hattermann, T., Nicholls, K. W., Hellmer, H. H., Davis, P. E., Janout, M. A., Østerhus, S., Schlosser, E., Rohardt, G., and Kanzow, T.: Observed interannual changes beneath Filchner-Ronne Ice Shelf linked to large-scale atmospheric circulation, Nature Communications, 12, 2961, https://doi.org/10.1038/s41467-021-23131-x, 2021.

Hellmer, H. H. and Olbers, D. J.: A two-dimensional model for the thermohaline circulation under an ice shelf, Antarctic Science, 1, 325–336, https://doi.org/10.1017/S0954102089000490, 1989.

https://doi.org/10.5194/egusphere-2025-1942
Preprint. Discussion started: 24 June 2025

Hinkel, J., Church, J. A., Gregory, J. M., Lambert, E., Le Cozannet, G., Lowe, J., McInnes, K. L., Nicholls, R. J., van Der Pol, T. D., and Van De Wal, R.: Meeting user needs for sea level rise information: A decision analysis perspective, Earth's Future, 7, 320–337, https://doi.org/10.1029/2018EF001071, 2019.

Holland, D. and Holland, D.: On the rocks: The challenges of predicting sea level rise, Eos, 96, https://doi.org/10.1029/2015EO036667, 2015.

Holland, D., Hunter, J., Grosfeld, K., Hellmer, H., Jenkins, A., Morales Maqueda, M., Hemer, M., Williams, M., Klinck, J., and Dinniman, M.: The ice shelf-ocean model intercomparison project (ISOMIP), in: Eos Trans. AGU, 84, Fall Meet. Suppl., vol. 2003, pp. C41A–05, 2003.

Holland, D. M. and Jenkins, A.: Modeling thermodynamic ice–ocean interactions at the base of an ice shelf, Journal of physical oceanography, 29, 1787–1800, https://doi.org/10.1175/1520-0485(1999)029<1787:MTIOIA>2.0.CO;2, 1999.

Holland, P. R.: The transient response of ice shelf melting to ocean change, Journal of Physical Oceanography, 47, 2101–2114, https://doi.org/10.1175/JPO-D-17-0071.1, 2017.

Holland, P. R., Jenkins, A., and Holland, D. M.: The response of ice shelf basal melting to variations in ocean temperature, Journal of Climate, 21, 2558–2572, https://doi.org/10.1175/2007JCLI1909.1, 2008.

Hunter, J.: Specification for test models of ice shelf cavities, in: Technical Report June, Antarctic Climate & Ecosystems Cooperative Research Centre, 2006.

ICES, SCOR, and IAPSO: Tenth Report of the Join Panel on Oceanographic Tables and Standards (The Practical Salinity Scale 1978 and the International Equation of State of Seawater 1980), Tech. rep., UNESCO Technical Papers in Marine Science, 1981.

IOC, SCOR, and IAPSO: The international thermodynamic equation of seawater – 2010: Calculation and use of thermodynamic properties. Intergovernmental Oceanographic Commission, Manuals and Guides No. 56, UNESCO (English), 2010.

IPCC: Climate Change 2021: The Physical Science Basis. Contribution of Working Group I to the Sixth Assessment Report of the Intergovernmental Panel on Climate Change, Cambridge University Press, Cambridge, UK and New York, NY, USA, https://doi.org/10.1017/9781009157896, 2021.

Jackett, D. R. and Mcdougall, T. J.: Minimal adjustment of hydrographic profiles to achieve static stability, Journal of Atmospheric and Oceanic Technology, 12, 381–389, https://doi.org/10.1175/1520-0426(1995)012<0381:MAOHPT>2.0.CO;2, 1995.

Jackson, L., Hallberg, R., and Legg, S.: A parameterization of shear-driven turbulence for ocean climate models, J. Phys. Oceanog., 38, 1033–1053, https://doi.org/10.1175/2007JPO3779.1, 2008.

Janout, M. A., Hellmer, H. H., Hattermann, T., Huhn, O., Sültenfuss, J., Østerhus, S., Stulic, L., Ryan, S., Schröder, M., and Kanzow, T.: FRIS revisited in 2018: On the circulation and water masses at the Filchner and Ronne ice shelves in the southern Weddell Sea, Journal of Geophysical Research: Oceans, 126, e2021JC017 269, https://doi.org/10.1029/2021JC017269, 2021.

Jenkins, A.: A simple model of the ice shelf–ocean boundary layer and current, Journal of Physical Oceanography, 46, 1785–1803, https://doi.org/10.1175/JPO-D-15-0194.1, 2016.

Jenkins, A. and Holland, D.: Melting of floating ice and sea level rise, Geophysical Research Letters, 34, https://doi.org/10.1029/2007GL030784, 2007.

Jenkins, A., Nicholls, K. W., and Corr, H. F.: Observation and parameterization of ablation at the base of Ronne Ice Shelf, Antarctica, Journal of Physical Oceanography, 40, 2298–2312, https://doi.org/10.1175/2010JPO4317.1, 2010.

https://doi.org/10.5194/egusphere-2025-1942
Preprint. Discussion started: 24 June 2025

Jordan, J. R., Holland, P. R., Goldberg, D., Snow, K., Arthern, R., Campin, J.-M., Heimbach, P., and Jenkins, A.: Ocean-forced ice-shelf thinning in a synchronously coupled ice-ocean model, Journal of Geophysical Research: Oceans, 123, 864–882, https://doi.org/10.1002/2017JC013251, 2018.

Jourdain, N. C.: nicojourdain/NEMO_PARAMS_SIMU: NEMO material (including Favier et al. 2019), https://doi.org/10.5281/zenodo.2562731, 2019.

Jourdain, N. C., Mathiot, P., Merino, N., Durand, G., Le Sommer, J., Spence, P., Dutrieux, P., and Madec, G.: Ocean circulation and sea-ice thinning induced by melting ice shelves in the Amundsen Sea, Journal of Geophysical Research: Oceans, 122, 2550–2573, https://doi.org/10.1002/2016JC012509, 2017.

Jourdain, N. C., Molines, J.-M., Le Sommer, J., Mathiot, P., Chanut, J., de Lavergne, C., and Madec, G.: Simulating or prescribing the influence of tides on the Amundsen Sea ice shelves, Ocean Modelling, 133, 44–55, https://doi.org/10.1016/j.ocemod.2018.11.001, 2019.

Jourdain, N. C., Asay-Davis, X., Hattermann, T., Straneo, F., Seroussi, H., Little, C. M., and Nowicki, S.: A protocol for calculating basal melt rates in the ISMIP6 Antarctic ice sheet projections, The Cryosphere, 14, 3111–3134, https://doi.org/10.5194/tc-14-3111-2020, 2020.

Jourdain, N. C., Mathiot, P., Burgard, C., Caillet, J., and Kittel, C.: Ice shelf basal melt rates in the Amundsen Sea at the end of the 21st century, Geophysical Research Letters, 49, e2022GL100 629, 2022.

Kusahara, K. and Hasumi, H.: Modeling Antarctic ice shelf responses to future climate changes and impacts on the ocean, Journal of Geophysical Research: Oceans, 118, 2454–2475, https://doi.org/10.1002/jgrc.20166, 2013.

Kusahara, K., Tatebe, H., Hajima, T., Saito, F., and Kawamiya, M.: Antarctic sea ice holds the fate of antarctic ice-shelf basal melting in a warming climate, Journal of Climate, 36, 713–743, https://doi.org/10.1175/JCLI-D-22-0079.1, 2023.

Large, W. G., McWilliams, J. C., and Doney, S. C.: Oceanic vertical mixing: A review and a model with a nonlocal boundary layer parameterization, Reviews of geophysics, 32, 363–403, https://doi.org/10.1029/94RG01872, 1994.

Lax, P. and Wendroff, B.: Systems of conservation laws, Communications on Pure and Applied Mathematics, 13, 217–237, https://doi.org/10.1002/cpa.3160130205, _eprint: https://onlinelibrary.wiley.com/doi/pdf/10.1002/cpa.3160130205, 1960.

Leonard, B., MacVean, M., and Lock, A.: Positivity-preserving numerical schemes for multidimensional advection, Tech. rep., https://ntrs.nasa.gov/citations/19930017902, 1993.

Leonard, B., MacVean, M., and Lock, A.: The flux integral method for multidimensional convection and diffusion, Applied Mathematical Modelling, 19, 333–342, https://doi.org/10.1016/0307-904X(95)00017-E, 1995.

Leonard, B. P.: A stable and accurate convective modelling procedure based on quadratic upstream interpolation, Computer methods in applied mechanics and engineering, 19, 59–98, https://doi.org/10.1016/0045-7825(79)90034-3, 1979.

Li, Q., England, M. H., Hogg, A. M., Rintoul, S. R., and Morrison, A. K.: Abyssal ocean overturning slowdown and warming driven by Antarctic meltwater, Nature, 615, 841–847, https://doi.org/10.1038/s41586-023-05762-w, 2023.

Little, C. M., Gnanadesikan, A., and Oppenheimer, M.: How ice shelf morphology controls basal melting, Journal of Geophysical Research: Oceans, 114, https://doi.org/10.1029/2008JC005197, 2009.

Losch, M.: Modeling ice shelf cavities in a z coordinate ocean general circulation model, Journal of Geophysical Research: Oceans, 113, https://doi.org/10.1029/2007JC004368, 2008.

MacAyeal, D. R.: Thermohaline circulation below the Ross Ice Shelf: A consequence of tidally induced vertical mixing and basal melting, Journal of Geophysical Research: Oceans, 89, 597–606, https://doi.org/10.1029/JC089iC01p00597, 1984.

https://doi.org/10.5194/egusphere-2025-1942
Preprint. Discussion started: 24 June 2025

Madec, G., Bourdallé-Badie, R., Bouttier, P.-A., Bricaud, C., Bruciaferri, D., Calvert, D., Chanut, J., Clementi, E., Coward, A., Delrosso, D., Ethé, C., Flavoni, S., Graham, T., Harle, J., Iovino, D., Lea, D., Lévy, C., Lovato, T., Martin, N., Masson, S., Mocavero, S., Paul, J., Rousset, C., Storkey, D., Storto, A., and Vancoppenolle, M.: NEMO ocean engine, https://doi.org/10.5281/zenodo.3248739, 2019.

Malyarenko, A., Wells, A. J., Langhorne, P. J., Robinson, N. J., Williams, M. J., and Nicholls, K. W.: A synthesis of thermodynamic ablation at ice–ocean interfaces from theory, observations and models, Ocean Modelling, 154, 101 692, https://doi.org/10.1016/j.ocemod.2020.101692, 2020.

Marshall, J., Adcroft, A., Hill, C., Perelman, L., and Heisey, C.: A finite-volume, incompressible Navier Stokes model for studies of the ocean on parallel computers, Journal of Geophysical Research: Oceans, 102, 5753–5766, https://doi.org/10.1029/96JC02775, 1997.

Mathiot, P. and Jourdain, N. C.: Southern Ocean warming and Antarctic ice shelf melting in conditions plausible by late 23rd century in a high-end scenario, Ocean Science, 19, 1595–1615, https://doi.org/10.5194/os-19-1595-2023, 2023.

Mathiot, P., Jenkins, A., Harris, C., and Madec, G.: Explicit representation and parametrised impacts of under ice shelf seas in the z_* coordinate ocean model NEMO 3.6, Geoscientific Model Development, 10, 2849–2874, https://doi.org/10.5194/gmd-10-2849-2017, 2017.

McDougall, T. J., Jackett, D. R., Wright, D. G., and Feistel, R.: Accurate and computationally efficient algorithms for potential temperature and density of seawater, Journal of Atmospheric and Oceanic Technology, 20, 730–741, https://doi.org/10.1175/1520-0426(2003)20<730:AACEAF>2.0.CO;2, 2003.

McPhee, M. G.: An analytic similarity theory for the planetary boundary layer stabilized by surface buoyancy, Boundary-Layer Meteorology, 21, 325–339, https://doi.org/10.1007/BF00119277, 1981.

McPhee, M. G., Maykut, G. A., and Morison, J. H.: Dynamics and thermodynamics of the ice/upper ocean system in the marginal ice zone of the Greenland Sea, Journal of Geophysical Research: Oceans, 92, 7017–7031, https://doi.org/10.1029/JC092iC07p07017, 1987.

Mellor, G. L. and Yamada, T.: Development of a turbulence closure model for geophysical fluid problems, Reviews of Geophysics, 20, 851–875, https://doi.org/10.1029/RG020i004p00851, 1982.

Millero, F. J., Feistel, R., Wright, D. G., and McDougall, T. J.: The composition of Standard Seawater and the definition of the Reference-Composition Salinity Scale, 55, 50–72, https://doi.org/10.1016/j.dsr.2007.10.001, 2008.

Naughten, K. A., Meissner, K. J., Galton-Fenzi, B. K., England, M. H., Timmermann, R., and Hellmer, H. H.: Future projections of Antarctic ice shelf melting based on CMIP5 scenarios, Journal of Climate, 31, 5243–5261, https://doi.org/10.1175/JCLI-D-17-0854.1, 2018a.

Naughten, K. A., Meissner, K. J., Galton-Fenzi, B. K., England, M. H., Timmermann, R., Hellmer, H. H., Hattermann, T., and Debernard, J. B.: Intercomparison of Antarctic ice-shelf, ocean, and sea-ice interactions simulated by MetROMS-iceshelf and FESOM 1.4, Geoscientific Model Development, 11, 1257–1292, https://doi.org/10.5194/gmd-11-1257-2018, 2018b.

Naughten, K. A., Holland, P. R., and De Rydt, J.: Unavoidable future increase in West Antarctic ice-shelf melting over the twenty-first century, Nature Climate Change, 13, 1222–1228, https://doi.org/10.1038/s41558-023-01818-x, 2023.

Pacanowski, R. and Philander, S.: Parameterization of vertical mixing in numerical models of tropical oceans, Journal of Physical Oceanography, 11, 1443–1451, https://doi.org/10.1175/1520-0485(1981)011<1443:POVMIN>2.0.CO;2, 1981.

Pattyn, F., Schoof, C., Perichon, L., Hindmarsh, R., Bueler, E., De Fleurian, B., Durand, G., Gagliardini, O., Gladstone, R., Goldberg, D., et al.: Results of the marine ice sheet model intercomparison project, MISMIP, The Cryosphere, 6, 267–308, https://doi.org/10.5194/tc-6-573-2012, 2012.

Pattyn, F., Perichon, L., Durand, G., Favier, L., Gagliardini, O., Hindmarsh, R. C., Zwinger, T., Albrecht, T., Cornford, S., Docquier, D., et al.: Grounding-line migration in plan-view marine ice-sheet models: results of the ice2sea MISMIP3d intercomparison, Journal of Glaciology, 59, 410–422, https://doi.org/10.3189/2013JoG12J129, 2013.

https://doi.org/10.5194/egusphere-2025-1942
Preprint. Discussion started: 24 June 2025

Petersen, M., Asay-Davis, X., Jacobsen, D., Maltrud, M., Ringler, T., Van Roekel, L., and Wolfram, P.: MPAS Ocean User's Guide V6, https://doi.org/10.5281/zenodo.1246893, 2018.

Reed, B., Green, J. M., Jenkins, A., and Gudmundsson, G. H.: Recent irreversible retreat phase of Pine Island Glacier, Nature Climate Change, 14, 75–81, https://doi.org/10.1038/s41558-023-01887-y, 2024.

Reichl, B. G. and Hallberg, R.: A simplified energetics based planetary boundary layer (ePBL) approach for ocean climate simulations., Ocean Modell., 132, 112–129, https://doi.org/10.1016/j.ocemod.2018.10.004, 2018.

Richter, O., Timmermann, R., Gudmundsson, G. H., and De Rydt, J.: Coupling framework (1.0) for the Úa (2023b) ice sheet model and the FESOM-1.4 z-coordinate ocean model in an Antarctic domain, EGUsphere, 2024, 1–23, https://doi.org/10.5194/egusphere-2024-648, in review.

Rignot, E., Mouginot, J., Morlighem, M., Seroussi, H., and Scheuchl, B.: Widespread, rapid grounding line retreat of Pine Island, Thwaites, Smith, and Kohler glaciers, West Antarctica, from 1992 to 2011, Geophysical Research Letters, 41, 3502–3509, https://doi.org/10.1002/2014GL060140, 2014.

Ringler, T., Thuburn, J., Klemp, J., and Skamarock, W.: A unified approach to energy conservation and potential vorticity dynamics for arbitrarily-structured C-grids, Journal of Computational Physics, 229, 3065–3090, https://doi.org/10.1016/j.jcp.2009.12.007, 2010.

Ringler, T., Petersen, M., Higdon, R. L., Jacobsen, D., Jones, P. W., and Maltrud, M.: A multi-resolution approach to global ocean modeling, Ocean Modelling, 69, 211–232, https://doi.org/10.1016/j.ocemod.2013.04.010, 2013.

Roquet, F., Madec, G., McDougall, T. J., and Barker, P. M.: Accurate polynomial expressions for the density and specific volume of seawater using the TEOS-10 standard, Ocean Modelling, 90, 29–43, https://doi.org/10.1016/j.ocemod.2015.04.002, 2015.

Rosevear, M., Galton-Fenzi, B., and Stevens, C.: Evaluation of basal melting parameterisations using in situ ocean and melting observations from the Amery Ice Shelf, East Antarctica, Ocean Science, 18, 1109–1130, https://doi.org/10.5194/os-18-1109-2022, 2022.

Rosevear, M. G., Gayen, B., Vreugdenhil, C. A., and Galton-Fenzi, B. K.: How Does the Ocean Melt Antarctic Ice Shelves?, Annual Review of Marine Science, 17, 325–353, https://doi.org/10.1146/annurev-marine-040323-074354, 2025.

Sadai, S., Spector, R., DeConto, R., and Gomez, N.: The Paris Agreement and climate justice: inequitable impacts of sea level rise associated with temperature targets, Earth's Future, 10, e2022EF002 940, https://doi.org/10.1029/2022EF002940, 2022.

Scott, W. I., Kramer, S. C., Holland, P. R., Nicholls, K. W., Siegert, M. J., and Piggott, M. D.: Towards a fully unstructured ocean model for ice shelf cavity environments: Model development and verification using the Firedrake finite element framework, Ocean Modelling, 182, 102 178, https://doi.org/10.1016/j.ocemod.2023.102178, 2023.

Seroussi, H., Nowicki, S., Payne, A. J., Goelzer, H., Lipscomb, W. H., Abe-Ouchi, A., Agosta, C., Albrecht, T., Asay-Davis, X., Barthel, A., Calov, R., Cullather, R., Dumas, C., Galton-Fenzi, B. K., Gladstone, R., Golledge, N. R., Gregory, J. M., Greve, R., Hattermann, T., Hoffman, M. J., Humbert, A., Huybrechts, P., Jourdain, N. C., Kleiner, T., Larour, E., Leguy, G. R., Lowry, D. P., Little, C. M., Morlighem, M., Pattyn, F., Pelle, T., Price, S. F., Quiquet, A., Reese, R., Schlegel, N.-J., Shepherd, A., Simon, E., Smith, R. S., Straneo, F., Sun, S., Trusel, L. D., Van Breedam, J., van de Wal, R. S. W., Winkelmann, R., Zhao, C., Zhang, T., and Zwinger, T.: ISMIP6 Antarctica: a multi-model ensemble of the Antarctic ice sheet evolution over the 21st century, The Cryosphere, 14, 3033–3070, https://doi.org/10.5194/tc-14-3033-2020, 2020.

Shchepetkin, A. F. and McWilliams, J. C.: Correction and commentary for "ocean forecasting in terrain-following coordinates: Formulation and skill assessment of the regional ocean modeling system" by Haidvogel et al., 3595-3624, Journal of Computational Physics, 228, 8985–9000, https://doi.org/10.1016/j.jcp.2009.09.002, 2009.

https://doi.org/10.5194/egusphere-2025-1942
Preprint. Discussion started: 24 June 2025

Siahaan, A., Smith, R. S., Holland, P. R., Jenkins, A., Gregory, J. M., Lee, V., Mathiot, P., Payne, A. J., Ridley, J. K., and Jones, C. G.: The Antarctic contribution to 21st-century sea-level rise predicted by the UK Earth System Model with an interactive ice sheet, The Cryosphere, 16, 4053–4086, https://doi.org/10.5194/tc-16-4053-2022, 2022.

Skamarock, W. C. and Gassmann, A.: Conservative Transport Schemes for Spherical Geodesic Grids: High-Order Flux Operators for ODE-Based Time Integration, Monthly Weather Review, 139, 2962–2975, https://doi.org/10.1175/MWR-D-10-05056.1, 2011.

Smagorinsky, J.: General circulation experiments with the primitive equations: I. The basic experiment, Monthly weather review, 91, 99–164, https://doi.org/10.1175/1520-0493(1963)091<0099:GCEWTP>2.3.CO;2, 1963.

Smith, R., Jones, P., Briegleb, B., Bryan, F., Danabasoglu, G., Dennis, J., Dukowicz, J., Eden, C., Fox-Kemper, B., Gent, P., Hecht, M., Jayne, S., Jochum, M., Large, W., Lindsay, K., Maltrud, M., Norton, N., Peacock, S., Vertenstein, M., and Yeager, S.: The Parallel Ocean Program (POP) reference manual: Ocean component of the Community Climate System Model (CCSM), Tech. rep., Los Alamos National Laboratory, https://www2.cesm.ucar.edu/models/cesm1.2/pop2/doc/sci/POPRefManual.pdf, 2010.

Smith, R. S., Mathiot, P., Siahaan, A., Lee, V., Cornford, S. L., Gregory, J. M., Payne, A. J., Jenkins, A., Holland, P. R., Ridley, J. K., et al.: Coupling the UK Earth System Model to dynamic models of the Greenland and Antarctic ice sheets, Journal of Advances in Modeling Earth Systems, 13, e2021MS002 520, https://doi.org/10.1029/2021MS002520, 2021.

Smolarkiewicz, P. K. and Szmelter, J.: MPDATA: An edge-based unstructured-grid formulation, Journal of Computational Physics, 206, 624–649, https://doi.org/10.1016/j.jcp.2004.12.021, 2005.

Stern, A., Adcroft, A., Sergienko, O., and Marques, G.: Modeling tabular icebergs submerged in the ocean, Journal of Advances in Modeling Earth Systems, 9, 1948–1972, https://doi.org/10.1002/2017MS001002, 2017.

Stern, A., Adcroft, A., and Sergienko, O.: Modeling ice shelf cavities and tabular icebergs using Lagrangian elements, Journal of Geophysical Research: Oceans, 124, 3378–3392, https://doi.org/10.1029/2018JC014876, 2019.

Storkey, D., Blaker, A. T., Mathiot, P., Megann, A., Aksenov, Y., Blockley, E. W., Calvert, D., Graham, T., Hewitt, H. T., Hyder, P., Kuhlbrodt, T., Rae, J. G. L., and Sinha, B.: UK Global Ocean GO6 and GO7: a traceable hierarchy of model resolutions, Geoscientific Model Development, 11, 3187–3213, https://doi.org/10.5194/gmd-11-3187-2018, 2018.

Timmermann, R. and Hellmer, H. H.: Southern Ocean warming and increased ice shelf basal melting in the twenty-first and twenty-second centuries based on coupled ice-ocean finite-element modelling, Ocean Dynamics, 63, 1011–1026, https://doi.org/10.1007/s10236-013-0642-0, 2013.

Vaňková, I., Asay-Davis, X., Branecky Begeman, C., Comeau, D., Hager, A., Hoffman, M., Price, S. F., and Wolfe, J.: Subglacial discharge effects on basal melting of a rotating, idealized ice shelf, The Cryosphere, 19, 507–523, https://doi.org/10.5194/tc-19-507-2025, 2025.

Williams, M., Jenkins, A., and Determann, J.: Physical controls on ocean circulation beneath ice shelves revealed by numerical models, in: Ocean, ice and atmosphere: Interactions at the Antarctic continental margin (S Jacobs, R Weiss, eds) Antarctic Research Series, AGU, Washington DC, vol. 75, pp. 285–299, https://doi.org/10.1029/AR075p0285, 1998.

Yung, C. K., Rosevear, M. G., Morrison, A. K., Hogg, A. M., and Nakayama, Y.: Stratified suppression of turbulence in an ice shelf basal melt parameterisation, EGUsphere, 2024, 1–43, https://doi.org/10.5194/egusphere-2024-3513, in review.

Zhao, C., Gladstone, R., Galton-Fenzi, B. K., Gwyther, D., and Hattermann, T.: Evaluation of an emergent feature of sub-shelf melt oscillations from an idealized coupled ice sheet–ocean model using FISOC (v1. 1)–ROMSIceShelf (v1. 0)–Elmer/Ice (v9. 0), Geoscientific Model Development, 15, 5421–5439, https://doi.org/10.5194/gmd-15-5421-2022, 2022.

Zhou, Q. and Hattermann, T.: Modeling ice shelf cavities in the unstructured-grid, Finite Volume Community Ocean Model: Implementation and effects of resolving small-scale topography, Ocean Modelling, 146, 101 536, https://doi.org/10.1016/j.ocemod.2019.101536, 2020.

https://doi.org/10.5194/egusphere-2025-1942
Preprint. Discussion started: 24 June 2025

Zhou, Q., Zhao, C., Gladstone, R., Hattermann, T., Gwyther, D., and Galton-Fenzi, B.: Evaluating an accelerated forcing approach
1220 for improving computational efficiency in coupled ice sheet-ocean modelling, Geoscientific Model Development, 17, 8243—8265, https://doi.org/10.5194/gmd-17-8243-2024, 2024.